PROPRIETARY
INFORMATION

NASA

SBIR PHASE 1 FINAL REPORT

Investigation of Hypersonic Rarefied
Flow on a Spherical Nose of the AOTV

July 20, 1987

Prepared by:

Amolak C. Jain, PhD.
G. Hamilton Woods

Contract NAS8-37305

Prepared for:

National Aeronautics and Space Administration
George C. Marshall Space Flight Center
Marshall Space Flight Center, AL 35812

FOREWORD

This report presents the results of research performed at REMTECH's Huntsville office. The work was conducted for NASA Marshall Space Flight Center (MSFC) in response to Phase I requirements of SBIR Contract NAS8-37305.

NASA Technical Coordination for this study was provided by Mr. Werner K. Dahm of the Aerophysics Division (ED-31) of the Systems Dynamics Laboratory.

TABLE OF CONTENTS

TABLE OF CONTENTS (cont'd)

NATIONAL AERONAUTICS AND SPACE ADMINISTRATION
SBIR PHASE 1 FINAL REPORT

CONTRACT NO. NAS8-37305

PROJECT TITLE Investigation of Hypersonic Rarefied Flow on a Spherical Nose of the AOTV

PURPOSE The purposes of the Phase I effort were to develop the physical and mathematical models of the hypersonic rarefied flow on the forebody of the spherical nose of a reentry vehicle (AOTV/AFE) and to apply these models for investigating the structure of the flow on the forebody of the spherical nose of the AFE.

RESEARCH COMPLETED The Navier-Stokes equations have been integrated for investigating the flow characteristics on the blunt nose of a reentry vehicle. The stagnation line quantities were computed and used as boundary conditions for the axisymmetric code for the forebody flowfield solution. In order to demonstrate the influence of real gas effects on the flowfield solution, chemical kinetics were included. This chemistry model includes an option for wall catalycity effects. A set of computer codes incorporating these innovations was run for the spherical nose of the AFE for several points along its trajectory.

RESULTS The results of the Phase I investigation demonstrate the validity of the Navier-Stokes equations for solving flow over a blunt body in the transitional regime. The parametric studies performed provide useful qualitative data for assisting in the understanding of the aerothermodynamic properties of hypersonic rarefied flow. The results of the axisymmetric forebody cases help to clarify the structure of the flow on the forebody of a sphere.

POTENTIAL APPLICATIONS The computer codes developed in the Phase I effort can be used to model the flow over blunt bodies in the transitional flow regime, bridging the gap between the continuum solutions and the rarefied soltions. Few flight data exist in this regime, and experimental data are difficult and expensive to obtain. Therefore, these codes could assist in predicting flow characteristics such as heat transfer coefficients, surface temperatures, surface pressure, and drag on blunt nosed reentry vehicles and missiles.

NAME AND ADDRESS OF CONTRACTOR

REMTECH, Inc.
2603 Artie Street, Suite 21
Huntsville, AL 35805

PRINCIPLE INVESTIGATOR G. Hamilton Woods

ABSTRACT

We have integrated numerically the Navier-Stokes (NS) equations for investigating the flow characteristics on the forepart of the spherical nose of a space vehicle such as the AOTV or AFE by a modified Accelerated Successive Replacement (ASR) scheme under hypersonic rarefied conditions.[1] Technical feasibility of the mathematical approach has been demonstrated by computing the flowfield on a spherical nose under conditions that the AFE encounters at times t = 15 seconds and 20 seconds after its reentry into the atmosphere. Certain suggestions are made to improve the capability of the computer code for the follow-on investigation and research.

Local similar solutions for the merged layer flow along the stagnation line of the sphere had been developed by Jain and Adimurthy (AIAA J., Vol. 12, No. 3, 1974). These are correct to the same degree of accuracy as the NS equations. These solutions provided stagnation line boundary conditions for the domain of integration on the spherical nose. Also, a parametric study of the stagnation line solution has been made with a view to understand the flow characteristics in tunnels with different ambient fluids. Critical information about stagnation point aerothermal loads along the AFE trajectory have been obtained. Analytical expressions for surface slip temperature, jump conditions and concentration level in the presence of the real gas effects at the top of the Knudsen

---

[1]Research work on the problem was initiated while one of the investigators (ACJ) was a senior research associate (1983-85) at NASA Langley Research Center.

layer have been derived and used to calculate the stagnation line flowflield with nonequilibrium dissociation and ionization.

We have drawn a number of graphs to illustrate the basic physics of the flowfield, paying particular attention to the manner in which the shockwave structure in the outer region of the disturbed zone diffuses in the region downstream of the stagnation line and affects the viscous flow structure near the surface. Information about the variation of surface characteristics such as heat transfer, pressure and skin friction coefficients with the surface angle, θ, is provided for ready use by the designer.

The present analysis can be extended to include real gas effects and to bodies of arbitrary shapes. It shall further provide boundary conditions for integrating the NS equations in the near wake region.

NOMENCLATURE

$\bar{r}, \theta$ = Radial distance and vectorial angle from the center of the sphere respectively.

$\bar{u}, \bar{v}$ = Velocity components in θ- and $\bar{r}$- directions

$\bar{\rho}, \bar{p}, \bar{T}$ = Density, pressure and temperature respectively

$\bar{\mu}$ = Viscosity Coefficient

γ = Specific heat ratio (C_p/C_v)

C_p = Specific heat at constant pressure

C_v = Specific heat at constant volume

$\bar{r}_B$ = Body radius

η = Transformed Ordinate, $\dfrac{r-1}{r_e-1}$

Pr = Prandtl Number, $\dfrac{\bar{\mu} C_p}{\bar{K}}$

$\bar{K}$ = Thermal conductivity

Re_∞ = Free Stream Reynolds Number $\bar{\rho}_\infty \bar{u}_\infty \, \bar{r}_B / \bar{\mu} \, (\bar{T}_\infty)$

Re_O = Stagnation Reynolds Number, $\bar{\rho}_\infty \bar{u}_\infty \, \bar{r}_B / \bar{\mu} \, (\bar{T}_\bullet)$

$\bar{T}_O$ = Free-stream stagnation temperature

α, σ = Momentum and energy accommodations coefficients

M_∞ = Free-stream Mach Number

Λ = $\dfrac{1}{2} + \dfrac{1}{(\gamma-1)M_\infty^2}$

W = molecular weight of the mixture

W_i = molecular weight of species i

γ_i = Specific heat ratio for the species i

C_i = concentration of species i

NOMENCLATURE (Cont'd)

D_{ij} = Diffusion coefficient for species i with respect to the species j

D_{12} = binary diffusion coefficient

Le   = Lewis No., $\dfrac{\bar{\rho}\, C_{p_\infty}\, D_{12}}{\bar{k}}$

m_i = mass of the ith species

$d^j{}_k$ = diffusion vector for the jth species in the kth direction defined in eq. (2.26)

Subscripts:

∞ = Conditions in free-stream

O_∞ = Free-stream stagnation conditions

ω = Conditions at the wall

b   = Conditions at the top of the Knudsen layer

e   = Conditions at the outer edge of the merged-layer

s   = At the top of the Knudsen layer

1.0 INTRODUCTION

1.1 Identification and Significance of the Problem

The Aero-assisted Orbital Transfer Vehicle (AOTV) and the Aero-assisted Flight Experiment (AFE) vehicle have a blunt forebody followed by a cylindrical payload bay (1). Due to high rarefaction in the upper region of the atmosphere, there is a thick viscous layer on the forebody which may impinge on the payload bay and generate excessive heating. This reattachment of the flow at the bay may result in damage to the structure and termination of the mission.

The AOTV or AFE is supposed to fly in the upper rarefied region of the atmosphere for a sustained period of time. An accurate description of the aerodynamic characteristics (pitching/yawing moments) and aerothermal loads is critically important for the design of these vehicles. When real gas effects become important, the detailed information about the flow structure help us to calculate the blackout time and the ionized trail characteristics. Possibilities of designing a tunnel that can simulate the actual flight conditions are remote and actual flight data are extremely expensive to obtain. NASA is planning to fly the AFE vehicle in the transition regime which needs to be validated by accurate theoretical predictions.

1.2 Formulation of the Problem

When a vehicle flies in the rarefied regime of the atmosphere, the thick shockwave-like structure in the outer region of the disturbed zone merges smoothly with the inner viscous region near the body. The entire disturbed zone is termed here as Merged Layer (ML) flow. To investigate this ML regime on the forepart of the spherical nose of the AOTV or AFE we have integrated the full steady-state Navier-Stokes equations from the surface with surface slip and temperature jump boundary conditions to the freestream in the region bounded by the stagnation line (surface angle $\theta = 0.0$) and the boundary line with surface angle $\theta = 90^{\circ}$. Earlier attempts to solve the problem have been made by Victoria and Windhopf [2] and Li [3]. They based their mathematical description of the flow-field on the unsteady Navier-Stokes equations which builds viscosity in the computation and thus loses accuracy. Dogra and Moss [4] used the Direct Simulation Monte-Carlo Technique (DSMC) to calculate aerothermal loads on an AFE vehicle. The DSMC technique is essentially based on binary collisions and is time consuming on computers.

We have modified the Accelerated Successive Replacement (ASR) method [5] to solve the set of coupled, nonlinear partial differential equations governing the Navier-Stokes fluid flow. Computations have been carried out for AFE flight conditions at times of 15 seconds and 20 seconds of its reentry phase. The ASR method is found to be quite versatile to solve the complicated flow

equations. However, a few improvements in the method are yet to be made in Phase II of the research to make it robust. Of particular importance is the need to incorporate an adaptive grid-generation technique and to update the stagnation line solution with effects arising from the disturbances in the downstream portion of the body. The combined effect of these improvements is expected to reduce the computation time, to remove slight oscillations that persist in the present computation in the various quantities in a narrow zone near the stagnation line, and to make the numerical method robust in that it becomes capable of catching even a thin shockwave structure in the computations.

1.3 Stagnation Point Solution and its Relevance

The Navier-Stokes equations are elliptic in nature and need an accurate description of the boundary conditions along the surfaces bounding the domain of integration. Here, we shall describe the development of the boundary conditions along the stagnation line. A description of the boundary conditions on the rest of the surfaces is described in Section 3.

Consistent with the accuracy of the present formulations, Jain and Adimurthy (6,7) developed a semi-analytic stagnation line solution of the NS equations. They used the ASR method for numerical computation. The results agree with reasonable accuracy with the experimental data and with the DSMC calculations of Bird (8) up to Knudsen number = 0.6. Here, for use of computation, the downstream effects on the stagnation line are ignored. In Ref. 9, Jain

incorporated the downstream effects in the analysis and found that the improved results come closer to the experimental data of Boylan (10) and the DSMC calculations of Moss and Bird (11) for Shuttle flight conditions up to an altitude of 104.93 km. In the SBIR Phase II investigation, it is proposed to update the stagnation line solution with the downstream effects propagating upstream through the medium up to the stagnation line.

The stagnation line computer code, called here HML0, is modified to include various viscosity-temperature laws (see Table 1). We operated the HML0 computer code for conditions at different points .along the AFE trajectory with different viscosity-temperature laws and with various values of the specific heat ratio (γ) and Prandtl number. It is hoped that this parametric study will help us to understand the effect of different ambient gases in various tunnels on the flow characteristics. Also, different values of γ imbibe, to a certain extent, the effect of real gases (12). At the trajectory time equal to 40 seconds of AFE trajectory, the shockwave becomes thin in comparison to the characteristic dimension of the flowfield. As such, there are not enough grid-points in the shockwave structure zone. Unless an adaptive grid-generation technique is incorporated in the HMLO computer code, it is difficult to catch relatively thin shockwave structures in the denser region of the AFE trajectory. For the time being, we have another computer code called the Hypersonic Viscous Shock Layer (HVSL) code (13) to calculate the flowfield in

Table 1   Listing of Various Codes

CODE	VISCOSITY MODEL OPTION	CATALYTICITY OPTION	SLIP OPTION	GAS TYPE
HML0 ·	LINEAR SQUARE ROOT SUTHERLAND	NO	YES	IDEAL
HML0RG	SUTHERLAND SQUARE ROOT HANSEN	YES	YES	REAL
HSVL	SQUARE ROOT	NO	YES	IDEAL
HMLAXI	LINEAR SQUARE ROOT SUTHERLAND	NO	YES	IDEAL

the denser region of the AFE trajectory. With the HVSL code, we computed the flowfield up to the point of highest heating along the AFE trajectory. It is to be noticed from Fig. 19 that the HMLO and HVSL codes give almost the same value of the heat transfer coefficient at the 30 second time point of the AFE trajectory. In a way, the two codes HMLO and HVSL complemented each other.

1.4 Real Gas Effects on the Stagnation Line Solution

Under reentry conditions of the AFE vehicle, the freestream stagnation temperature is of the order of $50,000^{\circ}K$. As such, the real gas effects such as dissociation, ionization, and possibly radiation exercise significant effects on the structure of the flowfield. Depending on the material of the surface (catalytic, noncatalytic and partially catalytic), different species may or may not recombine on colliding with the wall. The value of the concentration level at the top of the Knudsen layer needs to be deduced. Also, surface slip and temperature jump conditions need to be modified due to the presence of different species in the flowfield.

We have rederived the analytical expressions for the surface slip, temperature jump and concentration level at the top of the Knudsen layer in order to resolve the controversy that arose over the calculations of Henricks (14) and Gupta et. al. (15). The results are used in the real gas stagnation point computer code of Jain-Kumar-Henricks (16) with suitable modifications pointed out in the test. The code so developed is termed HMLORG. The HMLORG code was run for conditions in the AFE trajectory at various time

periods. Various graphs are drawn to understand the changes in the structure of the real gas flow due to the change in altitude and provide some information to the designer of the vehicle under real-istic flight conditions. This section is added in order to show the capability of the ASR method to solve the governing equations that become stiff due to the presence of real gas effects.   This procedure can be extended to incorporate real effects in the flow-field in the foreregion of the spherical nose of the space vehicle.

For details of references cited here, reference is made to the monograph entitled "Reentry Aerodynamics" by Jain (17).

A number of graphs have been drawn to illustrate the basic na-ture of the fluid flow under different ambient conditions. Partic-ular attention has been paid to understand the structure of the outer shockwave-like region and its dispersion in the atmosphere as the fluid expands downstream of the stagnation line. Graphs are also drawn for flow profiles and surface characteristics to under-stand the roll of dissipation processes in the ML of the spherical nose. Results of this study provide the initial conditions of a surface angle θ = 90° for integrating the NS equation for in-vestigating the near wake structure of the flow.

2.0 MATHEMATICAL FORMULATION

2.1 Governing Equation of Motion

The non-dimensional form of the Navier-Stokes equations in spherical-polar coordinates with axial symmetry are the following:

Continuity equation:

$$\frac{\partial}{\partial r}(\rho v) + \frac{1}{r}\frac{\partial}{\partial \theta}(\rho u) + \frac{2}{r}\rho v + \frac{\rho u}{r}\cot\theta = 0 \qquad (2.1)$$

Radial momentum equation:

$$\rho\left(\frac{u}{r}\frac{\partial v}{\partial\theta} + v\frac{\partial v}{\partial r} - \frac{u^2}{r}\right) = -\frac{\partial p}{\partial r}$$

$$+ \frac{1}{Re_O}\left\{\frac{2}{3}\frac{\partial}{\partial r}\left[2\mu\left(\frac{\partial v}{\partial r} - \frac{v}{r}\right) - \frac{\mu}{r}\left(u\cot\theta + \frac{\partial u}{\partial\theta}\right)\right]\right.$$

$$+ \frac{1}{r}\frac{\partial}{\partial\theta}\mu\left[r\frac{\partial}{\partial r}\frac{u}{r} + \frac{1}{r}\frac{\partial v}{\partial\theta}\right]$$

$$+ \frac{1}{r}\mu\cot\theta\left[r\frac{\partial}{\partial r}\frac{u}{r} + \frac{1}{r}\frac{\partial v}{\partial\theta}\right]$$

$$\left.+ \frac{2\mu}{r^2}\left[2\left(r\frac{\partial v}{\partial r} - v\right) - u\cot\theta - \frac{\partial v}{\partial\theta}\right]\right\} \qquad (2.2)$$

Tangential momentum equation:

$$\rho\left(\frac{u}{r}\frac{\partial u}{\partial\theta} + v\frac{\partial u}{\partial r} + \frac{uv}{r}\right) = -\frac{1}{r}\frac{\partial p}{\partial\theta}$$

$$+ \frac{1}{Re_O}\left\{\frac{2}{r}\frac{\partial}{\partial\theta}\left[\frac{\mu}{r}\left(\frac{\partial u}{\partial\theta} + v\right) - \frac{\mu}{3r}\left(r\frac{\partial v}{\partial r} + 2v + \frac{\partial u}{\partial\theta} + u\cot\theta\right)\right]\right.$$

$$+ \frac{\partial}{\partial r}\left[\mu\left(r\frac{\partial}{\partial r}\frac{u}{r} + \frac{1}{r}\frac{\partial v}{\partial\theta}\right] + 3\mu\left[r\frac{\partial}{\partial r}\left(\frac{u}{r}\right) + \frac{1}{r}\frac{\partial v}{\partial\theta}\right]$$

$$+ \frac{2\mu \, \mathrm{Cot}\,\theta}{r^2} \left(\frac{\partial u}{\partial \theta} - u \, \mathrm{Cot}\,\theta \right) \Big\} \qquad (2.3)$$

Energy equation:

$$\rho \left(\frac{u}{r} \, \frac{\partial T}{\partial \theta} + v \, \frac{\partial T}{\partial r} \right) = \frac{1}{\Lambda} \left(v \, \frac{\partial p}{\partial r} + \frac{u}{r} \, \frac{\partial p}{\partial \theta} \right)$$

$$+ \frac{1}{\mathrm{Re}_O} \, \frac{1}{\mathrm{Pr}} \, \frac{1}{r} \left\{ \frac{\partial}{\partial r} \left(\mu r \cdot \frac{\partial T}{\partial r} \right) + \mu \, \frac{\partial T}{\partial r} + \frac{\mu \, \mathrm{Cot}\,\theta}{r} \, \frac{\partial T}{\partial \theta} \right.$$

$$\left. + \frac{\partial}{\partial \theta} \left(\frac{\mu}{r} \cdot \frac{\partial T}{\partial \theta} \right) \right\} + \frac{1}{\mathrm{Re}_O} \left\{ \mu \left[2 \left(\frac{\partial v}{\partial r} \right)^2 + \frac{2}{r^2} \left(\frac{\partial u}{\partial \theta} + v \right)^2 \right. \right.$$

$$+ \frac{2}{r^2} \, (v + u \, \mathrm{Cot}\,\theta)^2 + \left(r \, \frac{\partial}{\partial r} \, \frac{u}{r} + \frac{1}{r} \, \frac{\partial v}{\partial \theta} \right)^2 \Bigg]$$

$$- \frac{2}{3} \, \mu \left[\frac{2v}{r} + \frac{\partial v}{\partial r} + \frac{u \, \mathrm{Cot}\,\theta}{r} + \frac{1}{r} \, \frac{\partial u}{\partial \theta} \right]^2 \Bigg\} \qquad (2.4)$$

where

$$\Lambda = \frac{C_p T_{O_\bullet}}{U_\bullet{}^2} = \frac{1}{2} + \frac{1}{(\gamma - 1)M_\bullet{}^2}$$

Equation of state:

$$p = \frac{\gamma - 1}{\gamma} \, \rho \, T \qquad (2.5)$$

Here, the variables are non-dimensionalized as follows:

$$u = \frac{\bar{u}}{\bar{u}_\bullet} \quad , \quad v = \frac{\bar{v}}{\bar{u}_\bullet} \quad , \quad T = \frac{\bar{T}}{\bar{T}_{O_\bullet}} \quad , \quad \rho = \frac{\bar{\rho}}{\bar{\rho}_\bullet}$$

$$p = \frac{\bar{p}}{\bar{\rho}_\bullet \bar{u}_\bullet{}^2} \quad , \quad = \frac{\bar{\mu}(\bar{T})}{\bar{\mu}(\bar{T}_{O_\bullet})} \quad , \quad r = \frac{\bar{r}}{\bar{r}_B} \qquad (2.6)$$

$$Re_O = \frac{\bar{\rho}_\bullet \bar{u}_\bullet \bar{r}_B}{\bar{\mu}(\bar{T}_{O_\bullet})}$$

A bar over a quantity represents its dimensional value. Other symbols are defined in the nomenclature.

Boundary conditions are the following:

At the edge of the merged-layer ($r = r_e$),

$u = \mathrm{Sin}\,\theta$

$v = -\mathrm{Cos}\,\theta$

$\rho = 1$

$$T = 1 - \frac{1}{2\Lambda} \qquad (2.7)$$

$$p = \frac{1}{\gamma M_\bullet{}^2}$$

At the surface of the body ($r = 1$),

Slip velocity is

$$u_b = \sqrt{\frac{\pi\gamma}{2}}\;\frac{2-\alpha}{\alpha}\;\frac{M_\bullet}{Re_O}\;\frac{\mu}{\rho}\;\sqrt{\frac{T_\bullet}{T}}\left(\frac{\partial u}{\partial r} - \frac{u}{r}\right)_{r=1} \qquad (2.8a)$$

$$v_b = 0.0 \quad (2.8b)$$

and the temperature jump condition is

$$T_b = T_w + \sqrt{\frac{\pi \gamma}{2}} \; \frac{2-\sigma}{\sigma} \; \frac{2\gamma}{\gamma+1} \; \frac{M_\infty}{Re_O \, Pr} \; \frac{\mu}{\rho} \sqrt{\frac{T_\infty}{T}} \left(\frac{\partial T}{\partial r} \right)_{r=1} \quad (2.8c)$$

where T_w is the dimensionless prescribed temperature at the wall. For the no slip case, at the body surface ($r = 1$),

$$u = v = 0.0 \quad (2.8d)$$

and

$$T = T_w \quad (2.8e)$$

The surface slip conditions (2.8a) and (2.8c) are taken from Kennard (18). For a monatomic gas with translational degrees of freedom, $\gamma = 5/3$. For a diatomic gas with fully excited rotational and translational degrees of freedom, $\gamma = 7/5$. And for a diatomic gas with fully exited rotational, translational and vibrational degrees of freedom, $\gamma = 9/7$. When these values are substituted in equations (2.8a, c), we obtain expressions for slip and temperature jump conditions which are the same as equations (D33) and (D34 a, b, c) derived by Gupta, et. al. (15) by detailed considerations of molecular dynamics of real gas flows.

2.2   Transformation of Independent Variables

Independent variables (r, θ) are transformed to (η, θ) by the following relation:

$$\eta = \frac{r - 1}{n_e(\theta)} \quad \text{where } n_e(\theta) = r_e(\theta) - 1$$

$$\theta = \theta \quad (2.9)$$

Here, $n_e(\theta)$ is the ML thickness on the sphere which changes with the surface angle θ.

The transformed variables (η, θ) transform the physical domain in (r, θ) into a rectangular domain $(0 \leq \eta \leq 1, 0 \leq \theta \leq \theta \text{ max})$. They eliminate the need of changing the number of grid points with the change in the merged layer (ML) thickness due to expansion of the flow downstream of the stagnation line of the sphere. Here, $n_e(\theta)$ appears as a parameter in the governing equations, transformed to new independent variables. $n_e(\theta)$ needs to be prescribed in advance of computation either by prescribing the criterion that the flow variables from the ML match the freestream conditions smoothly or by fixing its value so far away that there is uniform flow in the outer region of the entire flow field. In the present work, it has been found expedient to use the latter approach. For the time being, we have fixed $n_e(\theta) = 1$ for $\theta \geq 0.0$ i.e. the ML thickness is the same as the body radius. However, we realize that there is need to develop a criterion that accommodates variation of the ML thickness with the surface angle, θ.

In the following derivation, we have kept n_e as a function of θ. This will enable us to relax the condition $n_e = $ constant for $\theta \geq 0$ in future development of the code.

The governing equations (2.1) to (2.5) and boundary conditions (2.7) and (2.8) are transformed from the physical (r, θ)-plane to the computational (η, θ)-plane in the following form:

The continuity equation becomes

$$\left(\frac{v}{n_e} - \frac{u}{1 + n_e\eta} \frac{\eta}{n_e} n_e' \right) \frac{\partial \rho}{\partial \eta} + \frac{u}{1 + n_e\eta} \frac{\partial \rho}{\partial \theta}$$

$$+ \left[\frac{1}{n_e} \frac{\partial v}{\partial \eta} + \frac{1}{1 + n_e\eta} \left(2v + u \cot\theta - \frac{\eta}{n_e} n_e' \frac{\partial u}{\partial \eta} + \frac{\partial u}{\partial \theta} \right) \right] \rho = 0 \qquad (2.10)$$

where

$$n_e' = \frac{d\, n_e}{d\, \theta}$$

The momentum equations and the energy equation become

$$A_1 \frac{\partial^2 v}{\partial \eta^2} + A_2 \frac{\partial^2 v}{\partial \eta \partial \theta} + A_3 \frac{\partial^2 v}{\partial \theta^2} + A_4 \frac{\partial v}{\partial \eta} + A_5 \frac{\partial v}{\partial \theta} + A_6 v + A_7 = 0 \qquad (2.11)$$

$$B_1 \frac{\partial^2 u}{\partial \eta^2} + B_2 \frac{\partial^2 u}{\partial \eta \partial \theta} + B_3 \frac{\partial^2 u}{\partial \theta^2} + B_4 \frac{\partial u}{\partial \eta} + B_5 \frac{\partial u}{\partial \theta} + B_6 u + B_7 = 0 \qquad (2.12)$$

$$C_1 \frac{\partial^2 T}{\partial \eta^2} + C_2 \frac{\partial^2 T}{\partial \eta \partial \theta} + C_3 \frac{\partial^2 T}{\partial \theta^2} + C_4 \frac{\partial T}{\partial \eta} + C_5 \frac{\partial T}{\partial \theta} + C_6 T + C_7 = 0 \qquad (2.13)$$

and the equations of state is

$$p = \frac{\gamma - 1}{\gamma} \Lambda \rho T \qquad (2.14)$$

Here, the coefficients A_i, B_i, C_i with i = 1 to 7 in equations (2.11) to (2.13) are written in the Appendix.

Surface boundary conditions for the slip case in transformed variables become

$$u_b = \sqrt{\frac{\pi \gamma}{2}} \quad \frac{2 - \alpha}{\alpha} \quad \frac{M_\infty}{Re_O} \quad \frac{\mu}{\rho}\sqrt{\frac{T_\infty}{T}} \left(\frac{1}{n_e} \frac{\partial u}{\partial \eta} - u \right)_{\eta = 0} \qquad (2.15a)$$

$$v_b = 0.0 \qquad (2.15b)$$

$$T_b = T_w + \sqrt{\frac{\pi \gamma}{2}} \cdot \frac{2 - \sigma}{\sigma} \cdot \frac{2 \gamma}{\gamma + 1} \cdot \frac{M_\infty}{Re_O \, Pr} \cdot \frac{\mu}{\rho}\sqrt{\frac{T_\infty}{T}} \left(\frac{1}{n_e} \cdot \frac{\partial T}{\partial \eta} \right)_{\eta = 0}$$

$$(2.15c)$$

For the no slip case,

$$u = v = 0 \qquad (2.15d)$$

and

$$T = T_w \qquad (2.15e)$$

2.3 **Stagnation Point Solution**

We obtain a particular solution of the governing equations (2.10) to (2.14) with boundary conditions (2.15) which is valid in the stagnation zone of the sphere. Here, the dynamic and thermodynamic variables are expanded around the axis of symmetry as follows:

	Zeroth Order Term	2nd Order Term	Higher Order Terms	
$u(\eta, \theta)$	$= u_O(\eta) \sin \theta$	$+ u_2(\eta) \sin^3 \theta$	$+ - - - - - -$	
$v(\eta, \theta)$	$= v_O(\eta) \cos$	$+ v_2(\eta) \cos\theta \sin^2 \theta$	$+ - - - - -$	
$\rho(\eta, \theta)$	$= \rho_O(\eta)$	$+ \rho_2(\eta) \sin^2 \theta$	$+ - - - - -$	(2.16)
$p(\eta, \theta)$	$= p_O(\eta) + p_2(\eta) \sin^2 \theta$	$+ p_4(\eta) \sin^4 \theta$	$+ - - - - -$	
$T(\eta, \theta)$	$= T_O(\eta)$	$+ T_2(\eta) \sin^2 \theta$	$+ - - - - - -$	
$\mu(\eta, \theta)$	$= \mu_O(\eta)$	$+ \mu_2(\eta) \sin^2 \theta$	$+ - - - - - -$	

where

$$\eta = \frac{r - 1}{r_e - 1}$$

and

$$r_e = r_{eo} + \eta_2 \sin^2 \theta$$

Here, r_{eo} denotes the thickness of the ML at the stagnation point and η_2 is the parameter that signifies the extent of variation of the ML thickness on the spherical surface from its value at the stagnation point. Both r_{eo} and η_2 are to be obtained as part of the computational procedure.

The form of the series expansion (2.16) is suggested by the form of the ML outer edge boundary conditions, the symmetry conditions about the axis and the fact that the Rankine-Hugoniot pressure behind the shockwave and the Newtonian pressure on the surface vary as $\sin^2 \theta$. Substituting the various expansions of the flow variables given by eqs. (2.16) in the set of governing eqs. (2.10) to (2.14) and the boundary conditions (2.15) and collecting terms of like powers of θ, we get ordinary differential equations and the boundary conditions for the various order terms in eqs. (2.16). A typical zeroth order equation is of the following form:

$$F (u_o, v_o, ..., u_2, v_2, ..., r_{eo}, \eta_2) = 0 \quad (2.17)$$

Mathematically, the second order terms in the zeroth order equation arise due to the elliptic nature of the governing equations and assymmetry in the ML outer edge from the spherical surface and represent corrections to the zeroth order equation. Physically, the presence of the second order terms in the zeroth order equation allows the stagnation point solution to realize the effect of what is happening downstream of the stagnation line. Terms like u_2, v_2, etc. represent the upstream propogation of disturbances from the downstream region of validity of the two term solution. The parameter η_2 is called, for lack of a better name, a spherical asymmetry parameter, because it arises due to the departure of the outer ML surface from the spherical body surface. These two effects, viz., the upstream propogation of disturbances in the stagnation zone and the spherical asymmetry of the ML outer surface, are termed here as downstream effects.

In Ref. (9), we investigated the downstream effects by evaluating the zeroth and second order terms in expansion (2.16) in an iterative manner and found that the results in the low Reynolds number regime with downstream effects come closer to the experimental data of Boylan (10) and to the results of DSMC calculations for the Shuttle flight trajectory points obtained by Moss and Bird (11).

In the present investigation, the downstream effects have been neglected. However, we realize that there is an urgent need to incorporate these effects so as to update the stagnation line

solution and thus predict the surface and flow quantities at the stagnation line accurately. Also, they may help us to remove oscillations that exist in the present computation up to a few points downstream of the stagnation line.

Neglecting the downstream effects, the equations governing the flow in the stagnation zone of a spherical body are the following:

$$\frac{1 + n_e\eta}{n_e} \left(\rho_0 v_0 \right)' + 2 \rho_0 (u_0 + v_0) = 0 \qquad (2.18)$$

$$\frac{v_0''}{n_e^2} = \frac{3}{4} \frac{Re_0}{\mu_0} \left(\frac{p_0'}{n_e} + \frac{\rho_0 v_0 v_0'}{n_e} \right) - \left(\frac{2}{1 + n_e\eta} + \frac{\mu_0'}{n_e \mu_0} \right) \frac{v_0'}{n_e}$$

$$- \frac{u_0}{2n_e(1 + n_e\eta)} + \left(\frac{\mu_0}{n_e \mu_0} + \frac{7}{2(1 + n_e\eta)} \right) \frac{u_0 + v_0}{1 + n_e\eta} \qquad (2.19)$$

$$\frac{p_2'}{n_e} = -\frac{1}{2} \frac{p_0'}{n_e} + \frac{\rho_0 u_0}{1 + n_e\eta} (u_0 + v_0) + \frac{1}{2} \frac{\rho_0 u_0 v_0'}{n_e} \qquad (2.20)$$

$$\frac{u_0''}{n_e^2} = \frac{Re_0}{\mu_0} \left\{ \frac{2p_2}{1 + n_e\eta} + \rho_0 \left[\frac{v_0 u_0'}{n_e} + \frac{u_0(u_0 + v_0)}{1 + n_e\eta} \right] \right\}$$

$$- \frac{u_0'}{n_e} \left(\frac{2}{1 + n_e\eta} + \frac{\mu_0'}{\mu_0 n_e} \right) + \frac{1}{3} \frac{v_0'}{n_e(1 + n_e\eta)}$$

$$+ \frac{u_0 + v_0}{1 + n_e\eta} \left(\frac{8}{3} \frac{1}{1 + n_e\eta} + \frac{\mu_0'}{\mu_0 n_e} \right) \qquad (2.21)$$

$$\frac{\Lambda}{n_e} (1 + n_e\eta)^2 \rho_o v_o T_o' = \frac{(1 + n_e\eta)^2}{n_e} v_o p_o'$$

$$+ \frac{1}{Re_o} \frac{1 + n_e\eta}{Pr} \left\{ \Lambda \left[2 \frac{\mu_o T_o'}{n_e} + \frac{1 + n_e\eta}{n_e^2} (\mu_o' T_o' + \mu_o T_o'') \right] \right\}$$

$$+ \frac{1}{Re_o} \frac{2(1 + n_e\eta)^2}{n_e^2} \mu_o v_o'^2 + \frac{4}{Re_o} \mu_o(u_o + v_o)^2$$

$$- \frac{2}{3} \frac{1}{Re_o} \mu_o \left[\frac{1 + n_e\eta}{n_e} v_o' + 2(u_o + v_o) \right]^2 \quad (2.22)$$

$$p_o = \frac{\gamma - 1}{\gamma} \Lambda \rho_o T_o \quad (2.23)$$

Here, a prime over a quantity represents its differentiation with respect to η, viz.

$$(\ ) = \frac{\partial}{\partial \eta} (\ )$$

Boundary conditions are the following:

At the outer edge of the ML, $\eta = 1.0$,

$$\left. \begin{array}{l} u_o = 1, \quad v_o = -1, \quad p_o = \frac{1}{\gamma M_\infty^2}, \quad p_2 = 0.0 \\ \\ \rho_o = 1, \quad T_o = 1 - \frac{1}{2\Lambda} \end{array} \right\} \quad (2.24)$$

For the slip case, at the body surface $\eta = 0$

$$u_o(1) = \sqrt{\frac{\pi\gamma}{2}} \frac{2 - \alpha}{\alpha} \frac{M_\infty}{Re_o} \frac{\mu}{\rho} \sqrt{\frac{T_\infty}{T}} \left(\frac{1}{n_e} \frac{\partial u_o}{\partial \eta} - u_o \right)_{\eta = 0}$$

$$(2.25a)$$

$$v_O(1) = 0$$

$$T_O(1) = \sqrt{\frac{\pi\lambda}{2}} \quad \frac{2-\sigma}{\sigma} \quad \frac{2\gamma}{\gamma+1} \quad \frac{M_\infty}{Re_O \; Pr} \quad \frac{\mu}{\rho} \sqrt{\frac{T_\infty}{T}} \left(\frac{1}{n_e} \frac{\partial T_O}{\partial \eta} \right)_{\eta \; = \; 0}$$

(2.25b)

For the no slip case, at the body surface, $\eta = 0$, at

$$u_O = v_O = 0 \; , \quad T = \bar{T}_w \quad (2.25c)$$

The equations (2.18) to (2.23) together with boundary conditions (2.24) and (2.25) are integrated by the Accelerated Sucession Replacement (ASR) method (5) to provide boundary conditions along the stagnation line of the domain of integration and initial conditions on the forepart of the spherical nose of a space vehicle. A brief outline of the numerical integration procedure is presented in the next section. In Ref. (7), it has been shown that the results from the above formulation agree reasonably well with the experimental data for the stagnation pressure distribution versus Reynolds number from Potter and Bailey (19), for the temperature profile by Ahouse and Bogdonoff (20) and for the density profile by Russel (21). In Ref. (7), it is concluded that the continuum approach based upon the full Navier-Stokes equations can be extended to surprisingly low Reynolds numbers. Detailed comparison of the present results (Ref. 13) with the DSMC calculation of Bird (8) showed that the continuum approach can be extended up to Kn. No. = 0.6. In Ref. (9), the present investigator showed good agreement of the present results with the DSMC calculations of Moss and Bird (11) for Shuttle flight conditions up to an altitude of 109.75 km. Further improvement and capability of the code is

possible by incorporating in it certain grid generation techniques which give adequate resolution of the flowfield in the regions of high gradients.

2.4 Real Gas Effects

The above description of the flow field is for an ideal gas where the dissociation, ionization and radiation phenomena are ignored for the sake of simplification in the analytical derivation and economy in computer time. However, in the actual flight condition of the AFE or AOTV, the free stream stagnation temperature is of the order of $50,000^{\circ}K$. Thus, the changes in the fluid properties due to real gas effects can no longer be ignored.

In Ref. (22), we introduced a finite rate chemistry model based upon the seven species (N2, O2, O, N, NO, NO^+, e) and six reactions with reaction rates given by Wray (23) in the fluid mechanical model of the previous section. We further assumed that vibrational degrees of freedom are in equilibrium with the translational temperature. Here, computations have been carried out using Hansen's viscosity law using multicomonent of diffusion of species and Sutherland viscosity law. Gamma, Prandtl number and Lewis number are constant at 1.4, 0.72 and 1.4 respectively. The governing equations of motion are given in Ref. (22). The same ASR method was used for numerical computation of the governing equation as was used for the ideal gas case.

In Ref. (22), we carried out the computations for the no slip boundary conditions. Scott (24) derived the slip boundary

conditions with finite-rate chemistry and wall catalyticity. Hendricks (25) modified these conditions to include the effect of a simple model of radiation and incorporated the same in the aero-thermochemical computer program of Jain and Kumar (22). Johnston and Henricks introduced a multi-component diffusion viscosity model and documented their findings in Ref. 16. Gupta et.al. (15) found that Hendricks has calculated the diffusion vector inaccurately. The present investigator reviewed the slip boundary conditions and found that in the diffusion vector,

$$
d_k^j = \frac{\rho^2}{n^2 m_j} \left(\frac{1}{m} \frac{\partial C_j}{\partial X_k} - C_j \sum_{q=1}^{NS} \frac{1}{m_q} \frac{\partial C_q}{\partial X_k} \right) \qquad (2.26)
$$

Hendricks (25) has neglected the second term in comparison to the first term. This approximation may be justified as $C_i < 1$ and the second term is second order in smallness in comparison to the first. We rederived the slip, temperature and concentration jump boundary conditions with full diffusion vector and put them in the following simple analytical form:

$$
C_i^S = \frac{2 - \gamma_i}{2 \gamma_i} \frac{M_\bullet}{Re_O} \frac{Le}{Pr} \frac{W_i}{W} \sqrt{\frac{2 \pi \gamma_i W_i}{W}} \frac{\mu}{\rho} \sqrt{\frac{T_\bullet}{T}}
$$

$$
\cdot \left[\frac{\partial C_i}{n_e \partial \eta} + (1 - C_i) \sum_{q=1}^{NS} \frac{W}{W_q} \frac{\partial C_q}{n_e \partial \eta} \right] \qquad (2.27)
$$

In Ref. 26, Gupta evaluated C_i from the second term of the diffusion vector, viz. $(1 - C_i) \sum_{q=1}^{NS} \frac{W}{W_q} \frac{\partial C_q}{n_e \partial \eta}$ and relaxed C_i appearing on the left hand side of the above equation.

$$u_s = \sqrt{\frac{\pi\gamma}{2}} \quad \frac{2-\alpha}{\alpha} \quad \frac{M_\bullet}{Re_O} \quad \frac{\mu}{\rho}\sqrt{\frac{T_\bullet}{T}} \left(\frac{1}{n_e} \quad \frac{\partial u}{\partial \eta} - u \right)_{\eta=0} \Bigg/$$

$$\sum_{i=1}^{NS} c_i^S \left(\frac{W}{W_i}\right)^{1/2} \qquad (2.28)$$

and

$$T_s = T_w + \Bigg\{ \sqrt{\frac{\pi\gamma}{2}} \quad \frac{2-\sigma}{\sigma} \quad \frac{M_\bullet}{Re_O} \quad \frac{1}{Pr} \quad \frac{\mu}{\rho}\sqrt{\frac{T_\bullet}{T}} \left[\frac{1}{2} \quad \frac{\gamma}{\gamma-1} \quad \frac{\partial T}{n_e \partial \eta} \right.$$

$$\left. + Le \left(T_w + \frac{5}{4} T_s \right) \sum_{i=1}^{NS} \left(\frac{\partial c_i}{n_e \partial \eta} + (1 - c_i) \sum_{q=1}^{NS} \frac{W}{W_q} \frac{\partial c_q}{n_e \partial \eta} \right) \right] \Bigg\} \Bigg/$$

$$\sum_{i=1}^{NS} \frac{c_i^S}{\left(\frac{W_i}{W}\right)^{1/2}} \qquad (2.29)$$

In the above derivations, we have made the following assumptions:

(i) Derivatives of the tangential component of velocity in the tangential direction and those of the normal component of velocity in the normal direction are negligible.

(ii) Multi-component diffusion coefficients, D_{ij}, are replaced by the binary diffusion coefficient, D_{12}.

In Ref. (22), results from the present improved formulation without slip conditions have been compared with the corresponding results of Dellinger which are based upon the truncated Navier-Stokes equations and found significant changes in the predictions of electron density and other flow quantities throughout the ML regime from Dellinger's results. Johnston and Hendricks (16) used the present code with surface slip conditions to calculate heat loads on the external tank of the Shuttle trajectory.

In the present investigation, we have made the ideal gas computer program of Section 2.2 operative with the real gas effects described in Ref. (22). The surface slip, temperature, and concentration jump conditions derived in eqs. (2.27) to (2.29) were included with a view to indicate the capability of the present approach to incorporate the real gas effects. This enabled the investigators to appreciate the wall catalyticity effects and to understand the physics of the flow field with finite-rate chemistry. For the time being, we have computed the results for flight conditions that the AFE encounters at time t = 15, 20, 25, and 30 seconds of its trajectory.

2.5 Hypersonic Viscous Shock-Layer Flow

The hypersonic merged layer (HML0) code described in Section 2.3 gives accurate results up to Knudsen number = 0.01. As the space vehicle descends deeper in the denser region of the atmosphere, the shock wave becomes infinitesimally thin and the present code with uniform grids does not allow enough grid-points to predict the shockwave structure with reasonable accuracy. With this in mind, we preferred to use another computer code in the denser region of the atmosphere. This code is based upon the Navier-Stokes equations truncated on the basis of the order of magnitude consideration and using Rankin-Hugoniot shock relations modified with transport effects and surface slip conditons. Analysis is developed along the lines of the HML0 code in that a series solution in the form of eqs. (2.16) is assumed and the ASR method

of integration is applied. The details of the method are given in Ref. (13). This computer code so developed is called the Hypersonic Viscous Shock-layer code and will be referred to in this report as HVSL.

In the present investigation, we have drawn a few graphs to show that the HVSL computer code can take over in the region of the AFE trajectory where the HML0 computer code becomes difficult to operate and it can predict flow and surface quantities right up to the point on AFE trajectory where maximum heating occurs, viz., t = 90 seconds. The two codes, viz., HML0 and HVSL complement each other and give capability to predict flow and surface quantities on the entire AFE trajectory.

3.0 NUMERICAL METHOD OF INTEGRATION

The Method of Accelerated Successive Replacement (ASR) essentially deals with the drawbacks in several numerical schemes which permit large changes in the flow variables in successive iterations. In certain cases, these changes continue to grow without limit as the iterations proceed and lead to the bursting of the numerical scheme. In the ASR method, we correct this situation by allowing the flow variables to change only by a small quantity in two successive iterations. We control the magnitude of changes at each grid point by an acceleration factor whose value changes from one grid point to another so as to achieve the above stated objectives. In each iteration the old value of a flow variables is replaced by its new value as soon as it is calculated. For the reasons stated here, the numerical method is called the Method of Accelerated Successive Replacement (ASR).

Liberstein (5) derived the ASR method for solving a mildly nonlinear algebraic equation. Lew (28) used it to solve the Falkner-Skan equation of boundary layer theory. Dellinger (27) solved coupled nonlinear ordinary differential equations resulting from the local similar solutions of thin shock layer equations. In the present investigation, we have aplied the ASR method to solve the stagnation point flow of an ideal gas as stated in Sec. 2.2 as well that of a real gas as described in Sec. 2.3. We then extended the applicability of the ASR method to solve coupled nonlinear
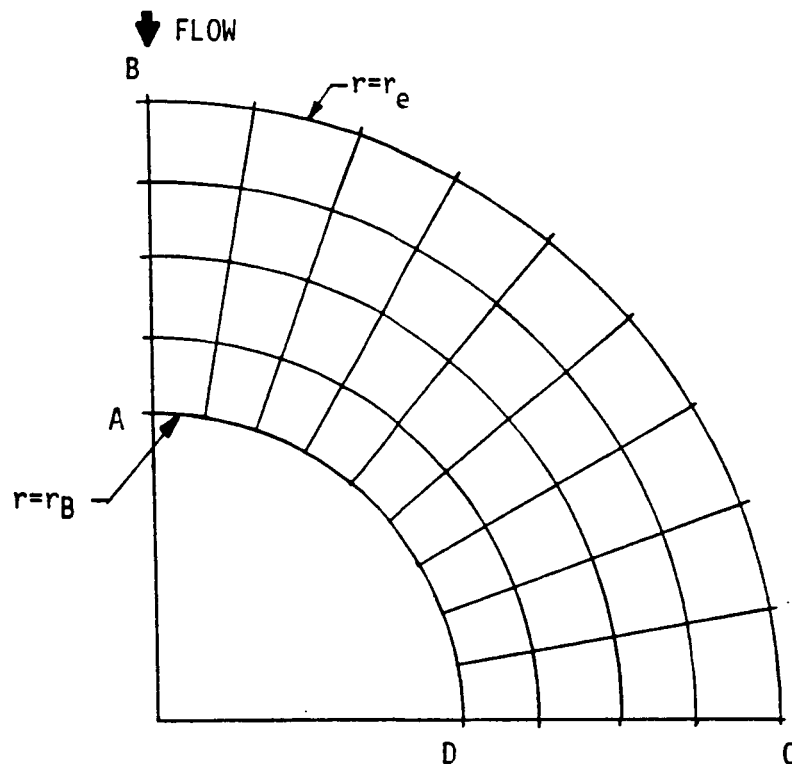
Navier-Stokes partial differental equations with split boundary conditions (Sec. 2.1).

The Navier-Stokes equations (2.1) to (2.5) with boundary conditions (2.8) are transformed to eqs. (2.10) to (2.15) from the physical (r, θ)-plane to the computational (η, θ)-plane through the transformation (2.9). The second order momentum and energy equations are changed to their finite-difference form using second order accurate central differences for the first order derivatives and the usual three point formula for the second order derivatives. To ensure consistently a second order accurate mathematical formulation, a three point one sided difference approximation for the first order derivative in the normal direction is used at the grid-points lying at either edge of the ML. The resulting set of finite-difference equations is solved at each grid point on a particular location on the spherical surface by the ASR method. The first order equation of continuity gives the density ρ. First order derivatives in the continutity equation are replaced by the forward-difference approximation. It is integrated from the outer ML edge immersed in the freestream to the surface. It is observed that, for an impermeable wall, there is a singularity in the value of the density at the surface. To circumvent the surface singularity in ρ, we evaluate the normal momentum equation at the surface ($\eta = 0$) and find the value of the normal pressure gradient, $\left(\dfrac{\partial p}{\partial \eta}\right)_{\eta=0}$. Then, using the results we
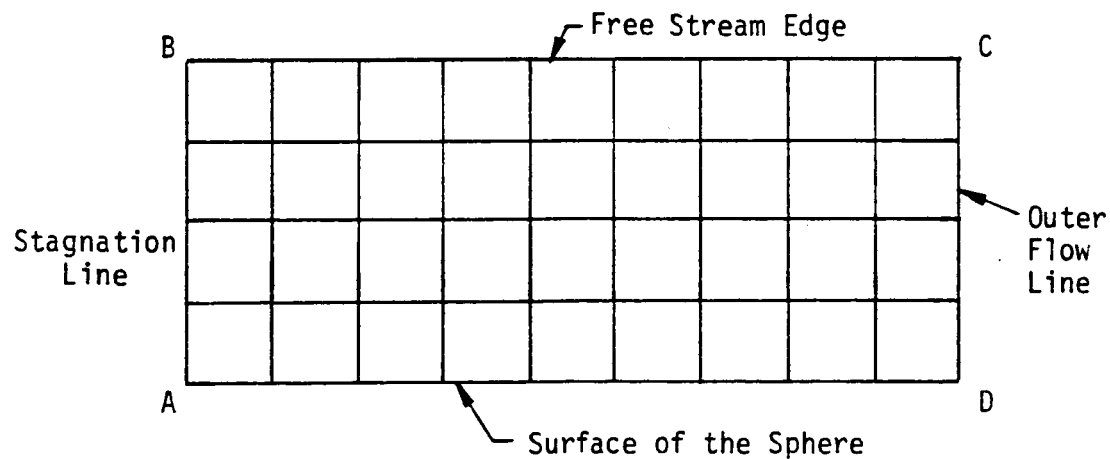
$$p(1) = p(2) - \left(\frac{\partial p}{\partial \eta}\right)_{\eta\,=0} x\ \Delta\eta, \ \Delta\eta \ \text{ being the grid size,}$$

find the value of pressure at the surface. Finally, the continuity equation gives the value of the surface density. The equation of state gives the pressure distribution at all other grid points in the flowfield.

We compute the flow properties in a zone bounded by the stagnation line AB, the line AD representing the surface of the sphere, the line BC in the freestream which lies at a sufficiently far off distance from the spherical surface and a line CD representing the outer limit of the domain of computation (Fig. 1). The line CD is generally termed as an outflow boundary. Since the governing equations are elliptic in nature, we need to prescribe boundary conditions for the dynamic and thermodynamic variables along each of the boundary lines of ABCD. Local similar solutions as discussed in Sec. 2.1 give the flow properties along the stagnation line AB and they also provide the initial conditions along the entire domain of integration. Surface slip and temperature jump conditions as derived in equation (2.15a) and (2.15c) provide conditions along AD. We prescribed the freestream conditions along the line BC and linearly extrapolated the flow variables u, v and T to obtain the flow conditions along the line CD. Also, along CD, density is given by the integration of the equation of continuity and pressure by the equation of state. Since the flow in the latter part of the free sphere has become supersonic, this linear extrapolation of the

FLOW

B

$r=r_e$

A

$r=r_B$

D   C

a) Physical Domain

Free Stream Edge

B   C

Stagnation
Line

Outer
Flow
Line

A   D

Surface of the Sphere

b) Computational Domain

Fig. 1   Physical and Computational Domains

flow variables along the outerflow boundary CD seems to represent correctly the physical situation.

We have divided the domain of integration into 26 x 150 grids of uniform size. The outer edge, BC, is supposed to lie at a distance of about a sphere radius so as to have a sufficient region of uniform flow towards the outer region in the entire domain of integration. Fine grids are taken to see the feasiblity of solving steady-state NS equations by the ASR method and thereby understand the basic nature of the hypersonic rarefied flows. However, there is need to optimize the grid size so as to reduce computation time.

4.0 DISCUSSION OF RESULTS

4.1 The Navier-Stokes Solutions on the Spherical Nose

We have drawn a number of graphs to illustrate the basic phy-
sics of the flow and to provide critical information to the
designer of the space vehicle about the manner in which the various
surface quantities vary with the distance down stream of the stag-
nation line as the vehicle descends from a rarer to a denser atmos-
phere. Particular attention is paid to the shockwave formation and
its dispersion in the atmosphere.

In Figs. 2 to 8, graphs are drawn for the tangential component
of velocity, temperature and pressure profiles at surface angles
θ = 0.0, 20.62°, 41.25°, 61.87°, and 82.5° on the forepart of the
spherical nose at times t = 15, 20 seconds of the AFE flight tra-
jectory. In this study, the surface temperature is held constant
at T_w = 0.2. Graphs for tangential velocity profiles in Fig. 2 at
time t = 15 seconds indicated fuller profiles and increase in slip
velocity as the surface angle, θ , increased. There is uniform
flow in the outer region of the domain of integration. The extent
of the uniform flow decreased as the surface angle, θ , decreased.
As the vehicle desended to the denser region at time t = 20 seconds
the zone of uniform flow in the outer region increased, indicating
a shrinkage of the ML thickness. There is no indication of a
shockwave-like structure in either of the Figs. 2 and 3.

In Figs. 4 and 5, graphs are drawn for the temperature pro-
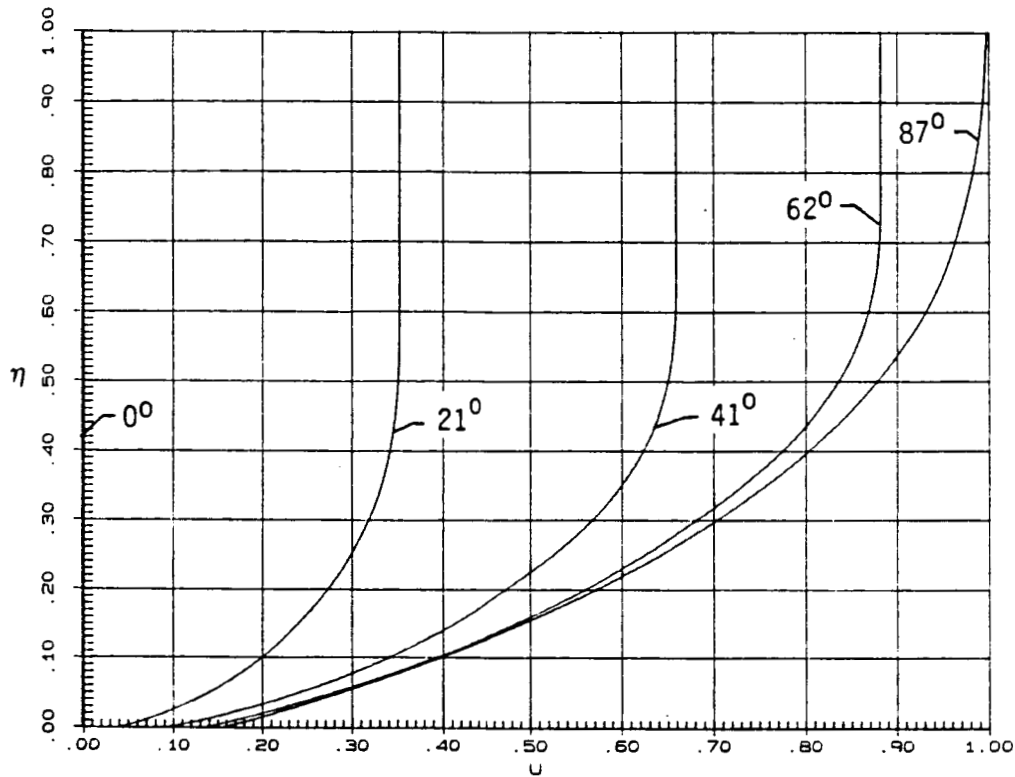files at times t = 15 seconds and 20 seconds of the AFE trajectory.

Fig. 2   Tangential Velocity Profiles at Time t = 15 Seconds of AFE
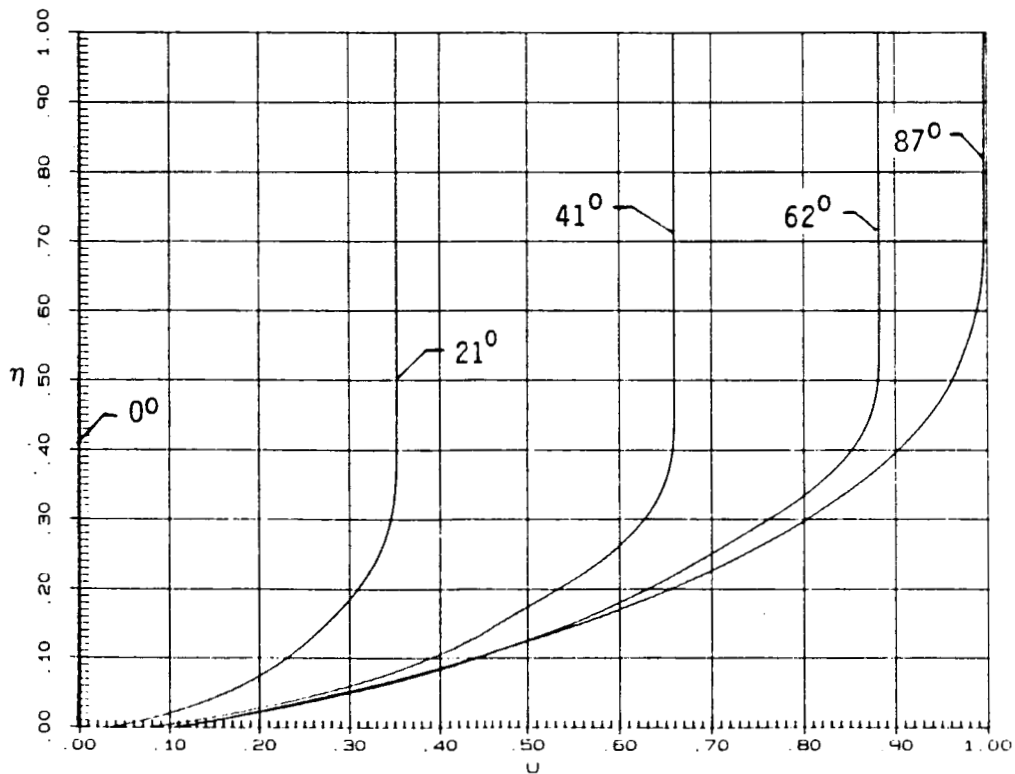   Flight Trajectory

Fig. 3   Tangential Velocity Profiles at Time t = 20 Seconds of the
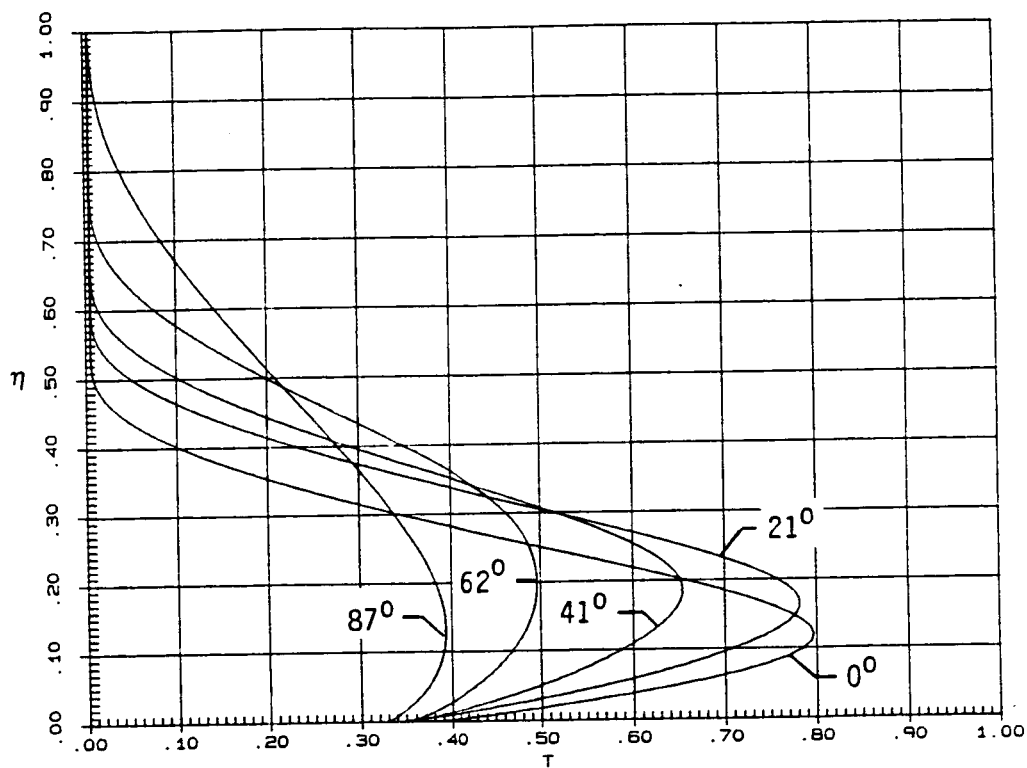   AFE Trajectory

Fig. 4   Temperature Profiles at Time t = 15 Seconds of the AFE Flight
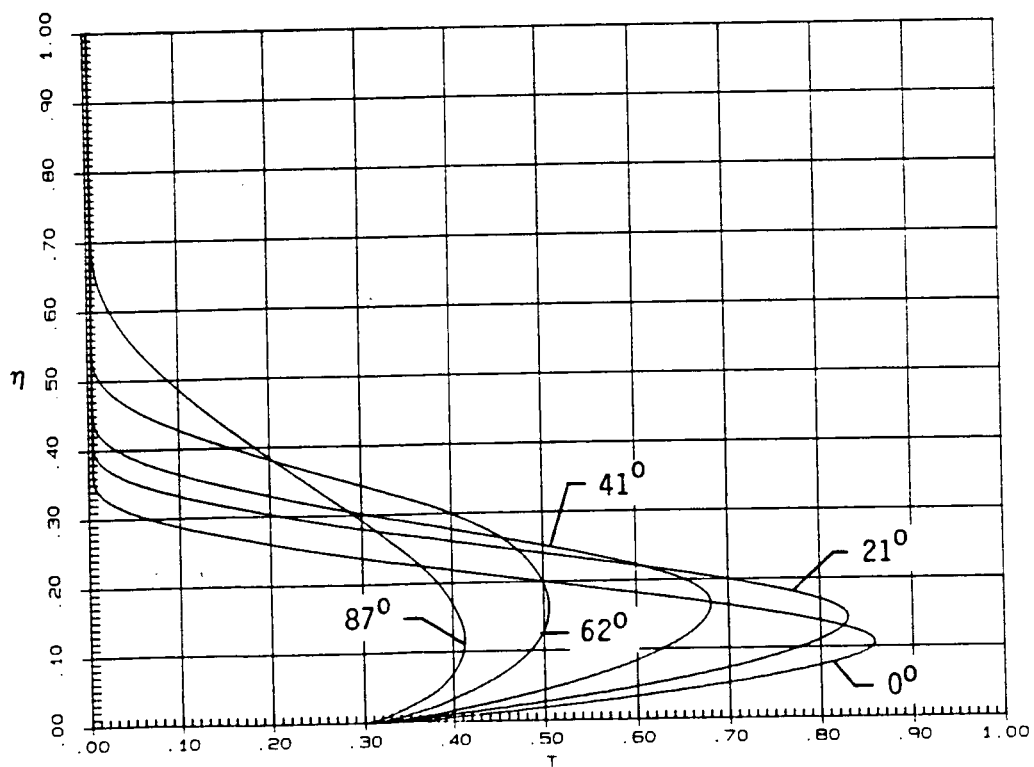   Trajectory

Fig. 5   Temperature Profiles at Time t = 20 Seconds of the AFE
          Trajectory

We found that the maximum temperature continually decreased and the surface slip temperature remained almost constant as the fluid moved from the stagnation line on the surface downstream. The peak in the temperature profiles is larger as the vehicle descended to time t = 20 seconds, indicating larger dissipative effects with greater ambient density. Let us interpret the shockwave-like structure as the zone lying in between the point of maximum temperature and the point where 99 percent of the freestream temperature is realized and the viscous layer as the fluid in the layer lying in between the maximum temperature and the surface. The two zones together form a merged layer (ML) on the spherical nose. We found that for large values of θ, ML thickness is of the order of the body radius. We observed from Fig. 6 that the viscous layer grew initially in extent in the stagnation zone and then shrank slightly in the aft portion of the sphere. Throughout the flow-field, the shockwave-like zone was several times the thickness of the viscous layer zone. In the aft portion of the sphere, the temperature profile showed a rounded shape, indicating a complete merging of the viscous layer and the shockwave-like structure. As a matter of fact, there is no shockwave-like zone for large values of θ. From a kinetic point of view, gas molecule and surface interactions dominate over molecule-molecule interactions. Hense, the effect of the body surface is realized throughout the flow-field. In the aft part of the spherical nose, molecule-molecule interactions dominate over the molecule-surface interactions, thus,
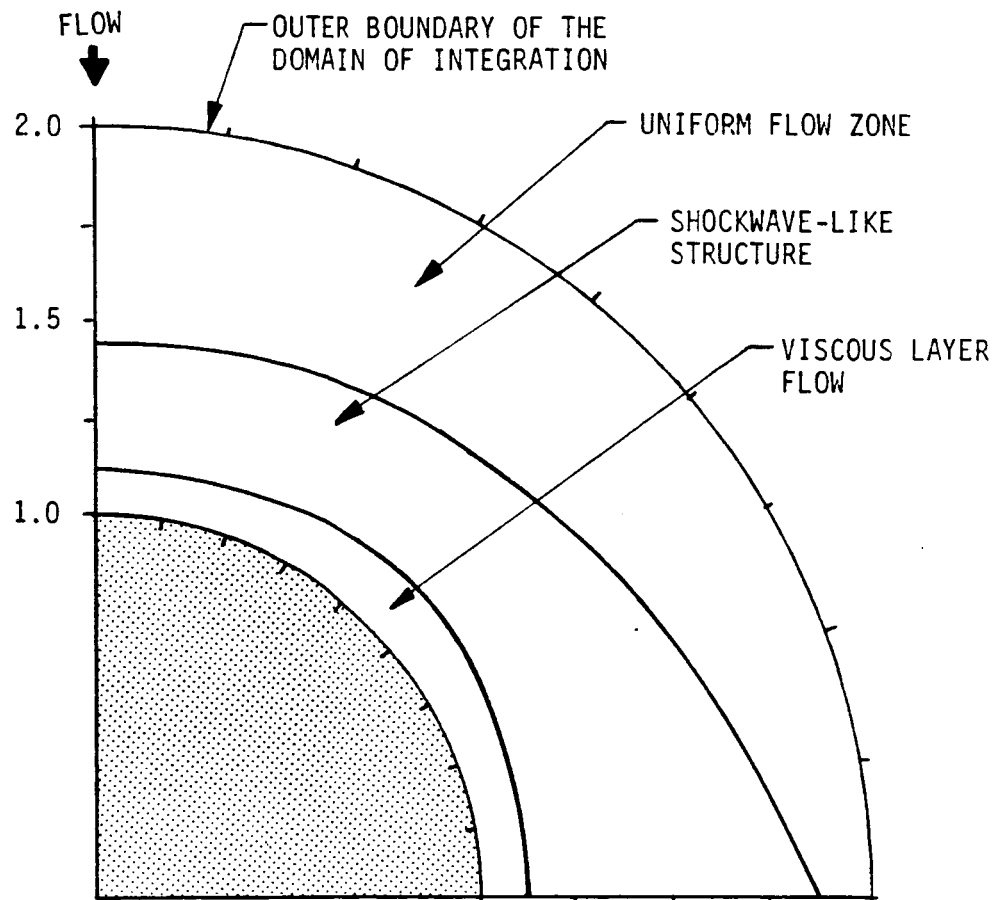
Fig. 6   Variation of the Shockwave-like Zone and Viscous Layer Zone with
Surface Angle, θ, of the AFE Flight Trajectory at t = 15
Seconds

giving rise to the excessive expansion of the flowfield and decreasing the wall effects in it.

In Figs. 7 and 8, we have drawn pressure profiles at various stations on the spherical nose of the vehicle under conditions that the AFE encounters at time t = 15 seconds and 20 seconds. On the forepart of the spherical nose, there are significant variations of pressure across the merged layer indicating a breakdown of the usual boundary layer assumption that the pressure gradient in the normal direction is negligible in comparision to the other quantities in the flowfield. Pressure variation near the surface becomes less severe as the fluid moves to the aft portion of the spherical nose. As the vehicle descended to the denser region at time t = 20 seconds, the severity in the normal pressure gradient decreased.

We observed that there were oscillations in the pressure profiles occuring downstream of the stagnation line in the region near the surface. The magnitude of the oscillations decreased as the fluid negotiated the aft spherical nose portion. These oscillations may be due to the fact that we have not updated the stagnatoin line solution in successive iterations. Disturbances from the downstream region propagate upstream through the subsonic portion of the ML flow and should modify the stagnation point flow. These may also be due to inadequacy of grid size near the wall or due to incorrect normal component of velocity. Density is evaluated from the continuity equation which becomes singular at the surface. In order to remove the singularity, we have to put certain restrictive
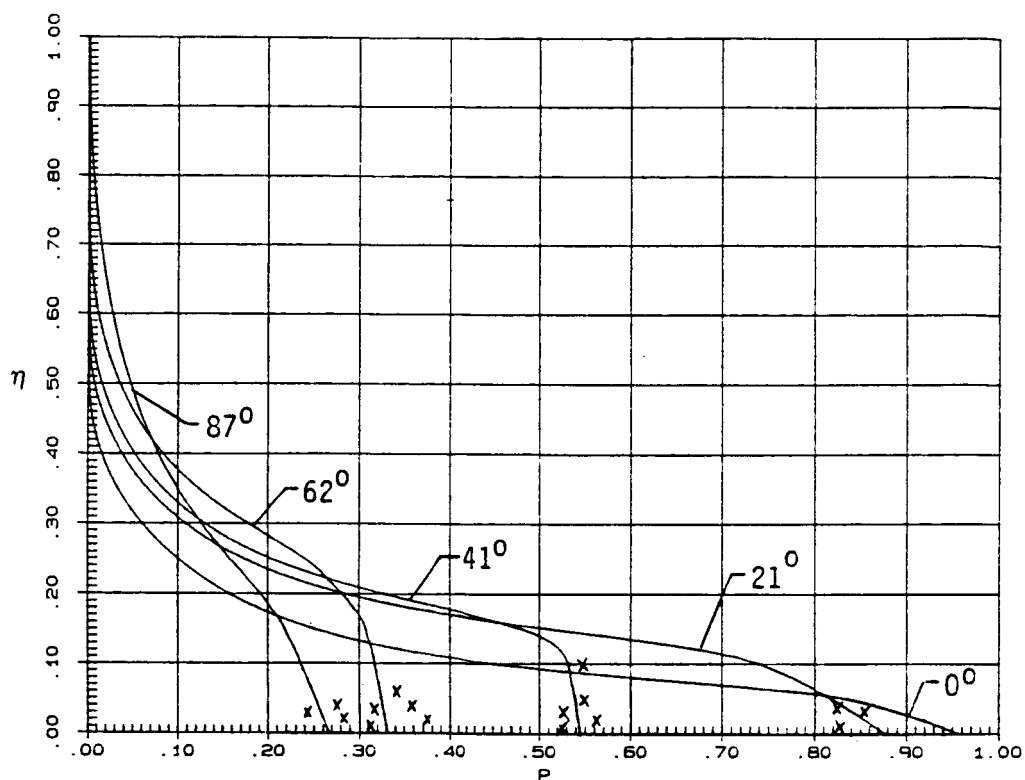
Fig. 7   Pressure Profiles at Time t = 15 Seconds of the AFE Flight
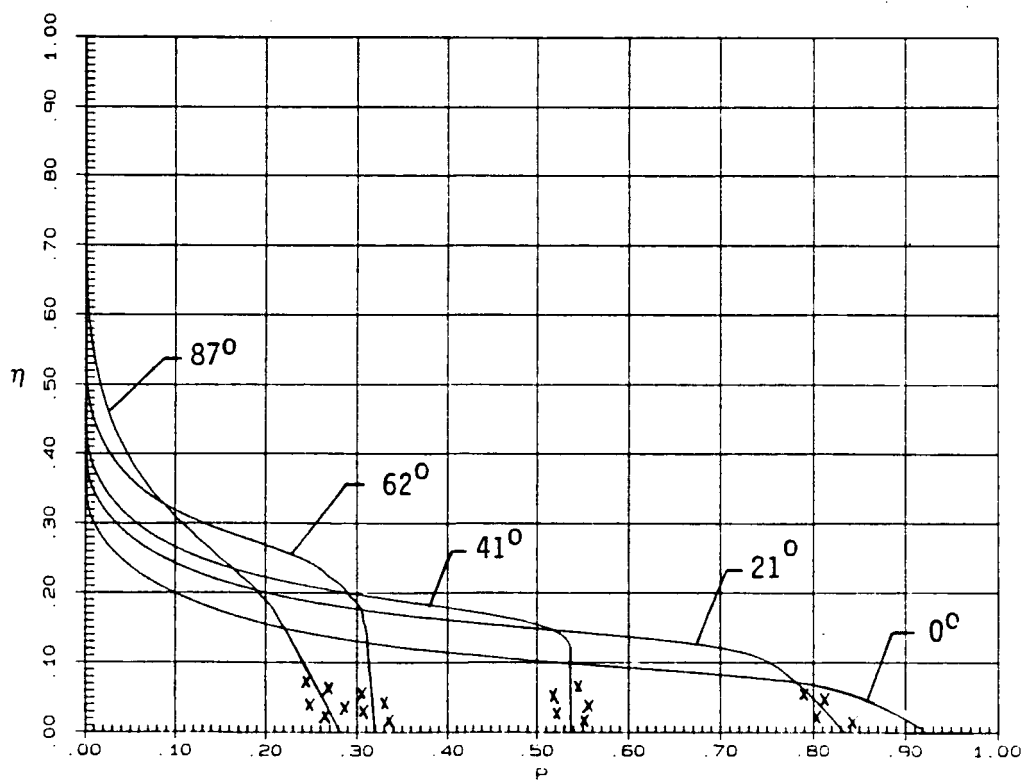   Trajectory

Fig. 8   Pressure Profiles at Time t = 20 Seconds of the AFE Flight
          Trajectory

conditions on the normal component of velocity. The oscillations near the wall were also observed in the density profile. Pressure is evaluated for the equation of state. Thus, the oscillations in the density profile feed themselves to the pressure profile. In the SBIR phase II effort, it is proposed to investigate the reasons for the oscillations in the pressure profile and remove them. It is hoped that these oscillations are local in nature and will not affect the overall characteristics of the flowfield.

In Figs. 9 and 10, we have drawn curves giving the variation of the heat transfer coefficient, C_H with the surface angle at times t = 15 seconds and 20 seconds of the AFE flight trajectory. Except for some oscillations at a few points downstream of the stagnation point, there is smooth variation of C_H with surface angle. These oscillations may again be due to our inability to incorporate downstream effects in the stagnation line solution. The heat transfer coefficient continually decreases with θ as the fluid expands and the shock becomes weak and diffused.

In Figs. 11 and 12, we have compared the skin friction coefficient and pressure distributions on the spherical nose at times t = 15 seconds and 20 seconds of the AFE trajectory. Except for some oscillations in the stagnation zone, there is smooth variation of C_F and p_w decreased in magnitude throughout the flowfield.

In Figs. 13 and 14, we have drawn the contours of constant density on the spherical nose for flight conditions at time t = 15 seconds and 20 seconds respectively and found a fast compression of
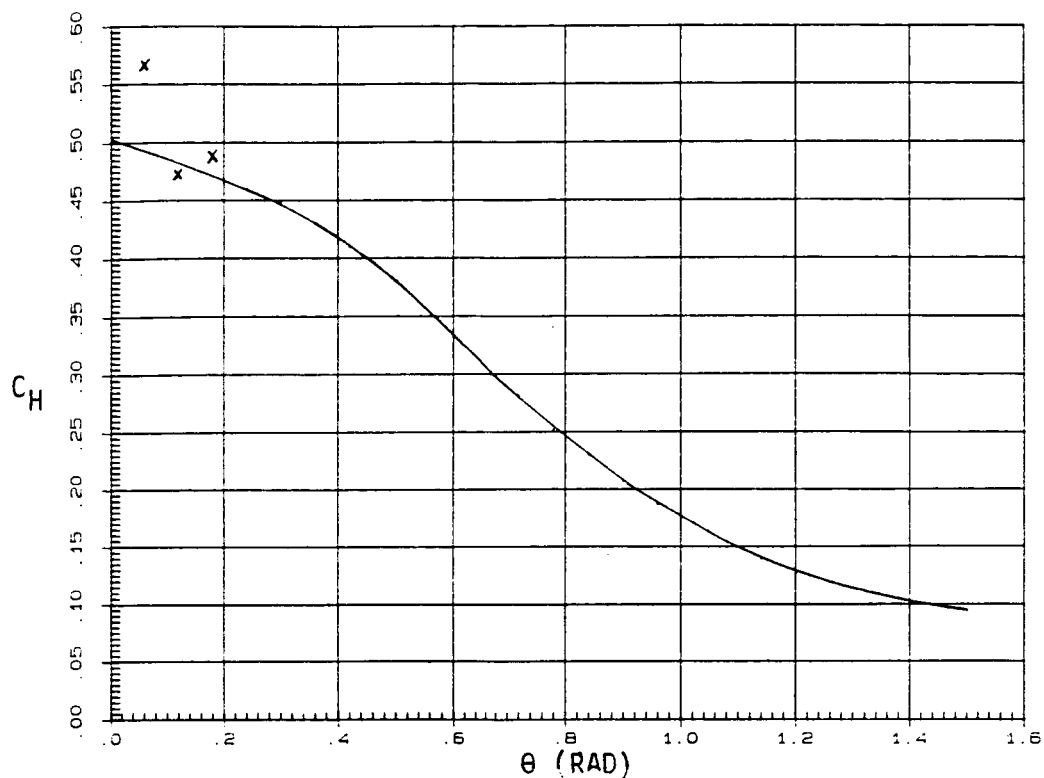
Fig. 9   Variation of Heat Transfer Coefficient, C_H, with Surface Angle
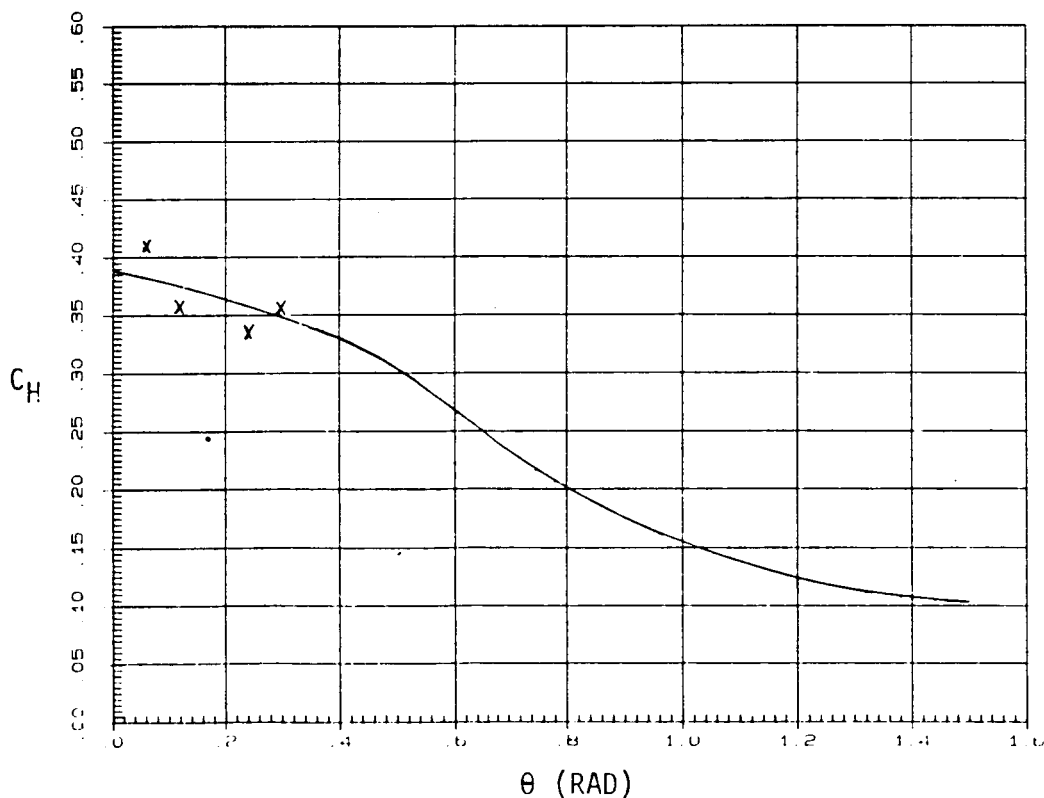θ at Time t = 15 Seconds of the AFE Flight Trajectory

Fig. 10   Variation of Heat Transfer Coefficient, C_H, with Surface Angle
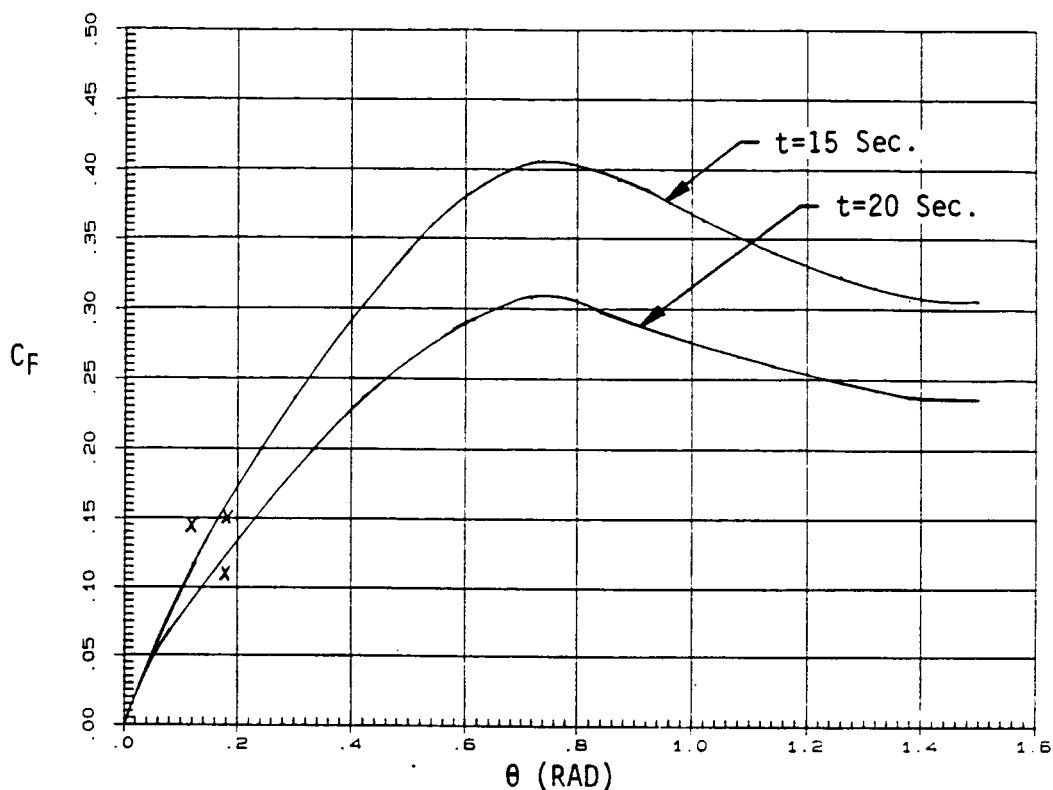θ at Time t = 20 Seconds of the AFE Flight Trajectory

Fig. 11   Comparison of Skin-Friction Coefficient, C_F, Distribution for
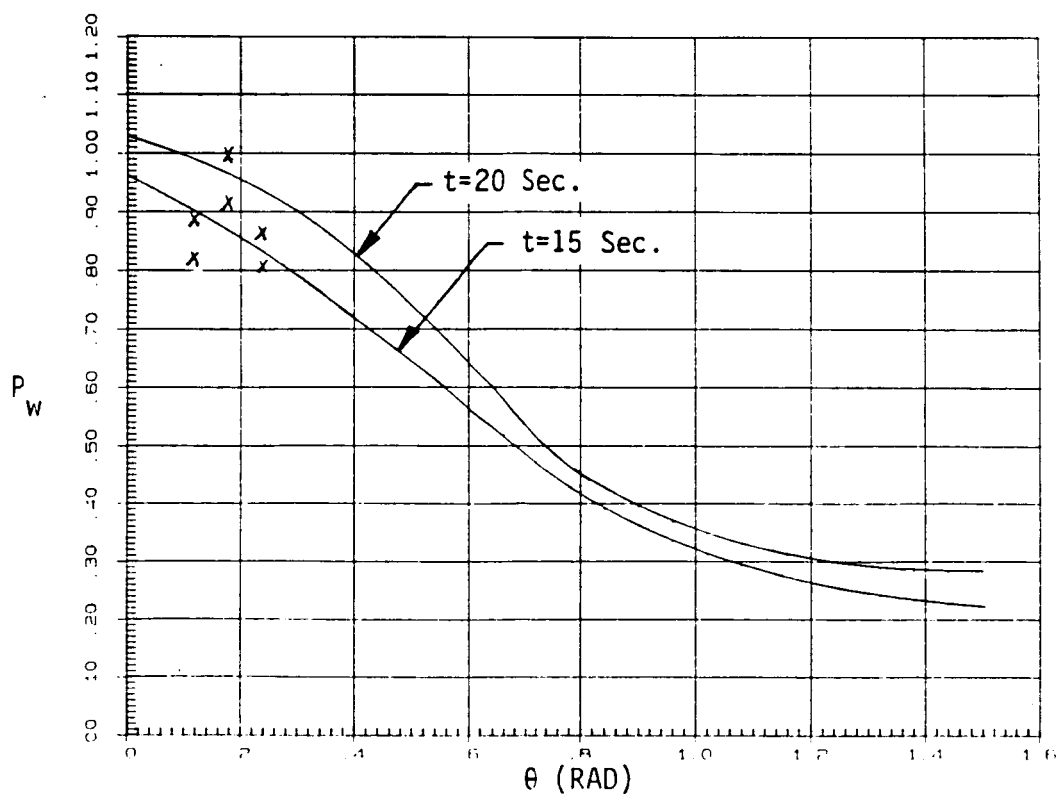Conditions at Time t = 15, 20 Seconds of the AFE Flight Trajectory

Fig. 12   Comparison of Pressure Distribution, P_w, on the Spherical
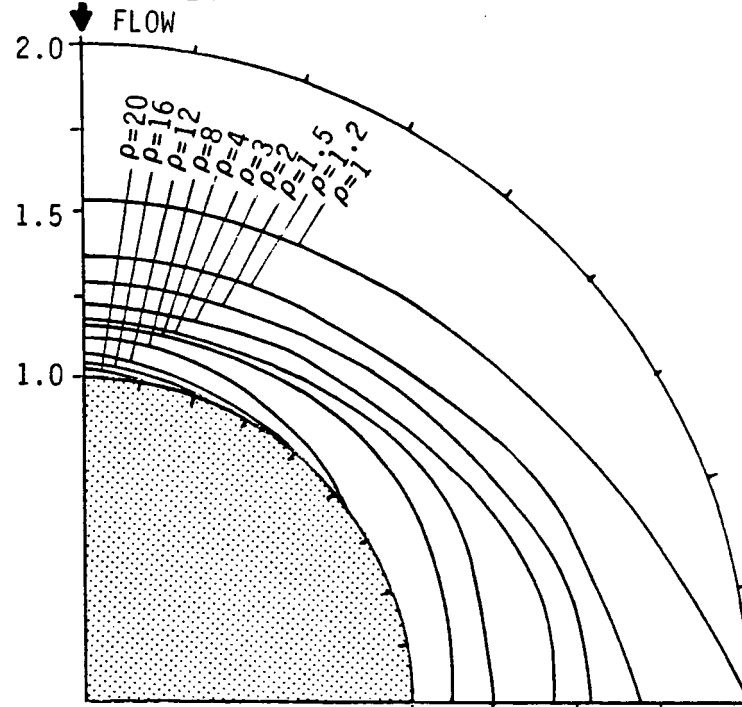Nose at Time t = 15 Seconds and 20 Seconds of the AFE Flight
Trajectory

- 39 -

Fig. 13   Contours of Constant Density on the Spherical Nose at Time
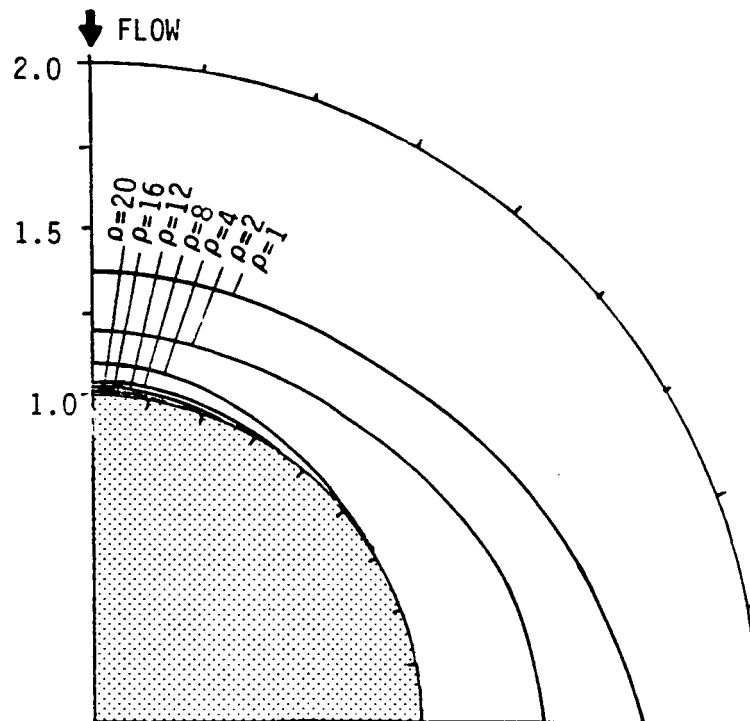t = 15 Seconds of the AFE Trajectory

Fig. 14   Contours of Constant Density on the Spherical Nose at Time
t = 20 Seconds of the AFE Trajectory

the fluid flow near the surface. In Figs. 15 and 16, contours of constant temperature are drawn for the two flight conditions mentioned above and the manner in which the maximum temperature moved down stream with the increase in the surface angle was observed. In Fig. 17, sonic lines for time t = 15 seconds and 20 seconds are drawn. The region between the sonic line and the surface is the subsonic zone which propagates disturbance upstream from the downstream portion of the flowfield. With an increase in the ambient density, the subsonic portion shrinks slightly in extent in the forepart of the spherical nose.

4.2 Stagnation Point NS Solution

The purpose of developing the stagnation point solution in Sec. 2.2 is to provide boundary conditions to the Navier-Stokes equations for their integration in the downstream region of the spherical nose. In Ref. 6, Jain and Adimurthy analyzed the local similar solutions governed by the zeroth order term of the asymptotic expansion (2.16) with and without surface slip boundary conditions (2.25). They found that the validity of the continuum can be extended to surprisingly low Reynolds numbers and validated the results by comparing them with the various experimental data (Refs. 19, 20, and 21) and the DSMC calculations of Bird (8). In Ref. 13, a detailed comparison with other theories is made and in Ref. 9, downstream effects are analyzed. The work done by the present investigator (ACJ) and his co-workers until 1980 is summarized in Ref. 17.
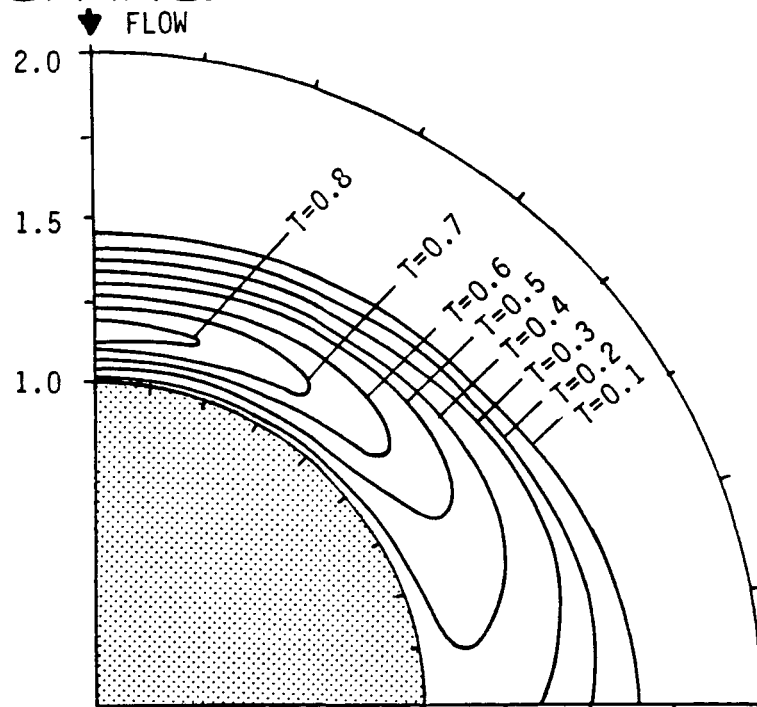
Fig. 15   Contours of Constant Temperature on the Spherical Nose at
Time t = 15 Seconds of the AFE Trajectory .
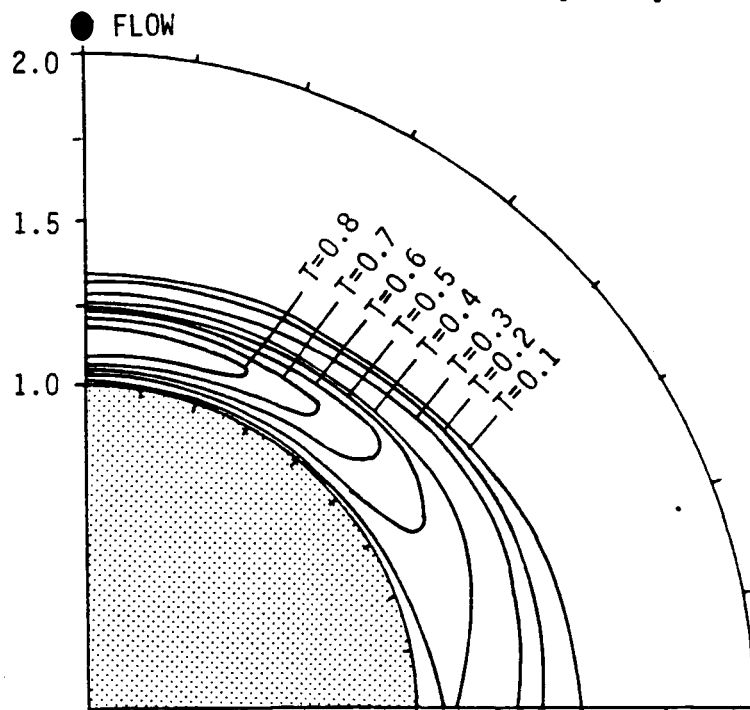

Fig. 16   Contours of Constant Temperature on the Spherical Nose at
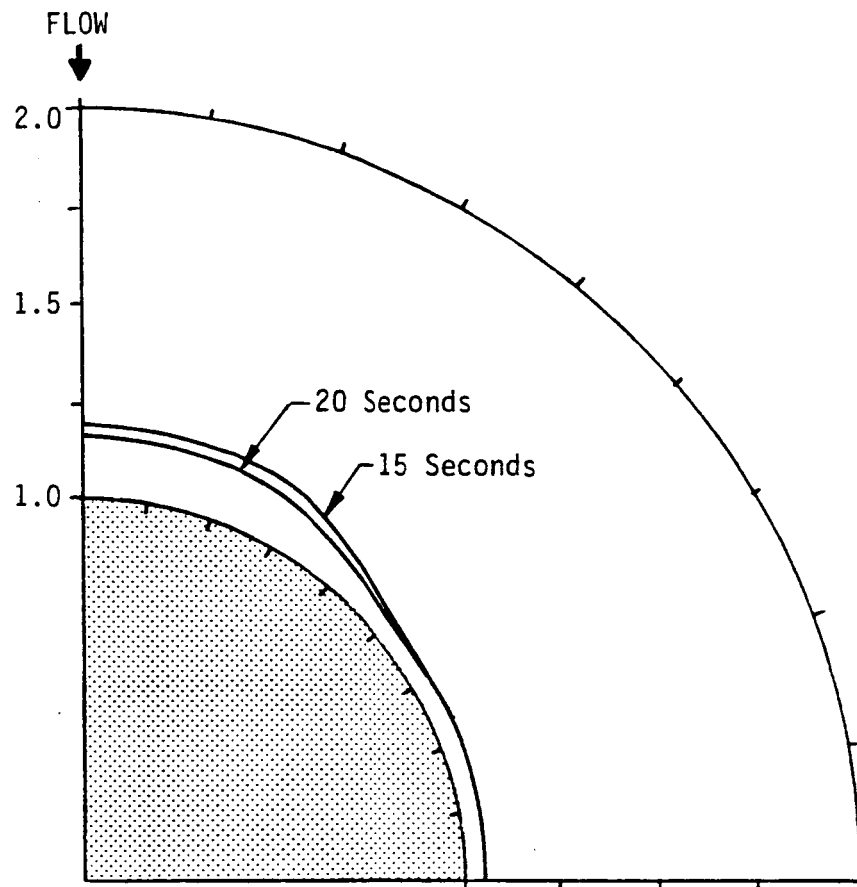Time t = 20 Seconds of the AFE Trajectory

FLOW

Fig. 17   Sonic Line Position on the Spherical Nose at Time t = 15
Seconds and 20 Seconds of the AFE Trajectory

So far, a few questions of practical importance were not answered. In different wind tunnels, there are different kinds of ambient fluids which have significantly different thermodynamic and transport properties. Also, to some extent, the effect of real gases in air can be imbibed in the ideal gas computations by the concept of effective γ (12). In the following, answers to these questions have been given with a view to provide the experimentalists with an idea of the directions the various flow and surface quantities will take when different fluids are used in wind tunnels.

In Figs. 18 to 21, the effects of different μ-T relations are studied. The test cases chosen were the conditions (see Table 2) encountered by the AFE vehicle at times t = 10, 20, 30 and 40 seconds during the early phases of its reentry into the atmosphere. Sutherland and square root viscosity temperature laws were chosen for computations. From Fig. 18, we observed that as the vehicles descended to the denser region of the atmosphere, the ML thickness decreased, the maximum temperature increased, the location of the maximum temperature shifted towards the surface, and the jump in surface temperature decreased. With the descent of the AFE vehicle, the reduction of the shockwave-like structure in the outer region of the ML is much faster than the reduction in the viscous layer thickness near the wall. At time t = 40 seconds (alt = 94.8 km), the shockwave is much thinner than the viscous layer thickness and the Rankine-Hugoniot relations are realized at the interface of

Table 2   Prescribed Conditions at Various Times in AFE Trajectory

TIME (SEC)	ALT (KM)	U_∞ (M/SEC)	T_∞ ($^\circ$K)	ρ_∞ (kg/m^3)	M_∞	Re_∞
10	114.3	9905	285.8	5.306×10^{-8}	29.22	74.77
15	110.5	9909	251.2	9.669×10^{-8}	31.19	151.0
20	107.2	9911	230.8	1.661×10^{-7}	32.54	278.0
25	103.9	9913	214.4	2.876×10^{-7}	33.77	511.7
30	100.6	9915	203.7	5.309×10^{-7}	34.66	986.9
35	97.7	9912	196.8	9.056×10^{-7}	35.25	1733.0
40	94.8	9909	191.7	1.513×10^{-6}	35.70	2961.0
45	92.3	9898	188.4	2.392×10^{-6}	35.97	4746.0
50	89.9	9886	186.7	3.712×10^{-6}	36.09	7414.0
55	87.7	9863	189.5	5.350×10^{-6}	35.74	10524.0
60	85.6	9832	191.5	7.615×10^{-6}	35.44	14799.0
65	83.9	9785	193.0	1.015×10^{-5}	35.14	19497.0
70	82.4	9539	194.0	1.354×10^{-5}	34.86	25249.0
75	81.2	9653	194.4	1.614×10^{-5}	34.53	30403.0
80	80.1	9569	195.5	1.927×10^{-5}	34.15	35815.0
85	79.4	9471	195.6	2.188×10^{-5}	33.78	40214.0
90	78.9	9365	196.2	2.386×10^{-5}	33.36	43260.0

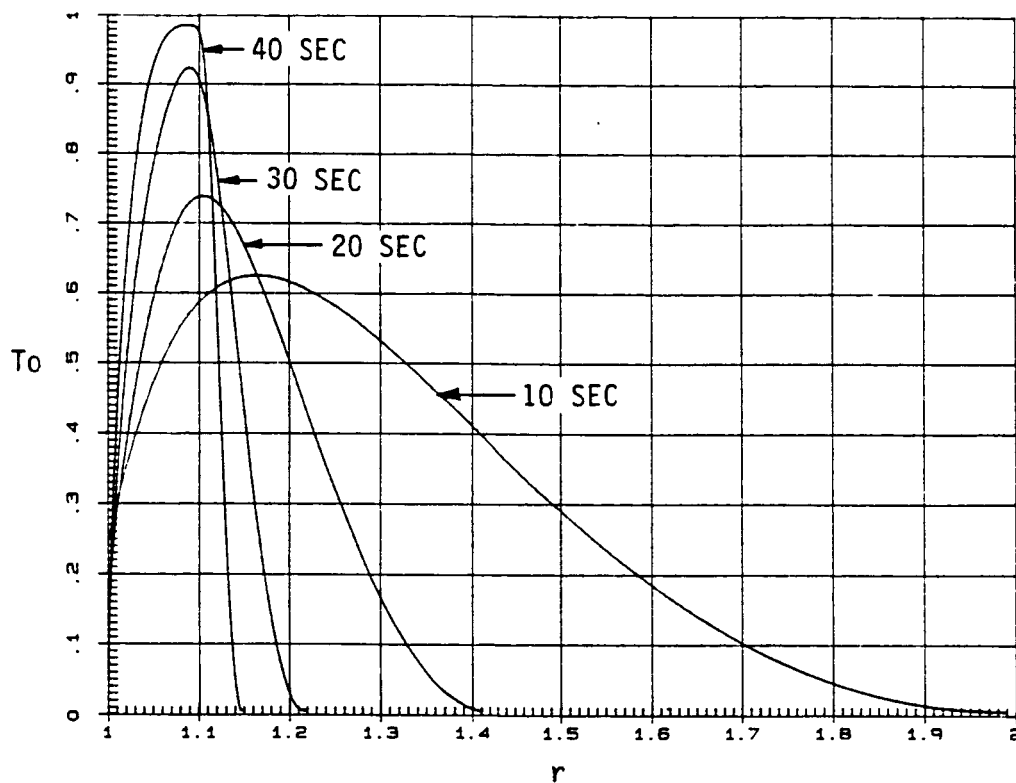Wall Temperature = 1111°K
Nose Radius = 2.53m

Fig. 18   Stagnation Point Temperature Profiles from HMLO Code at Time
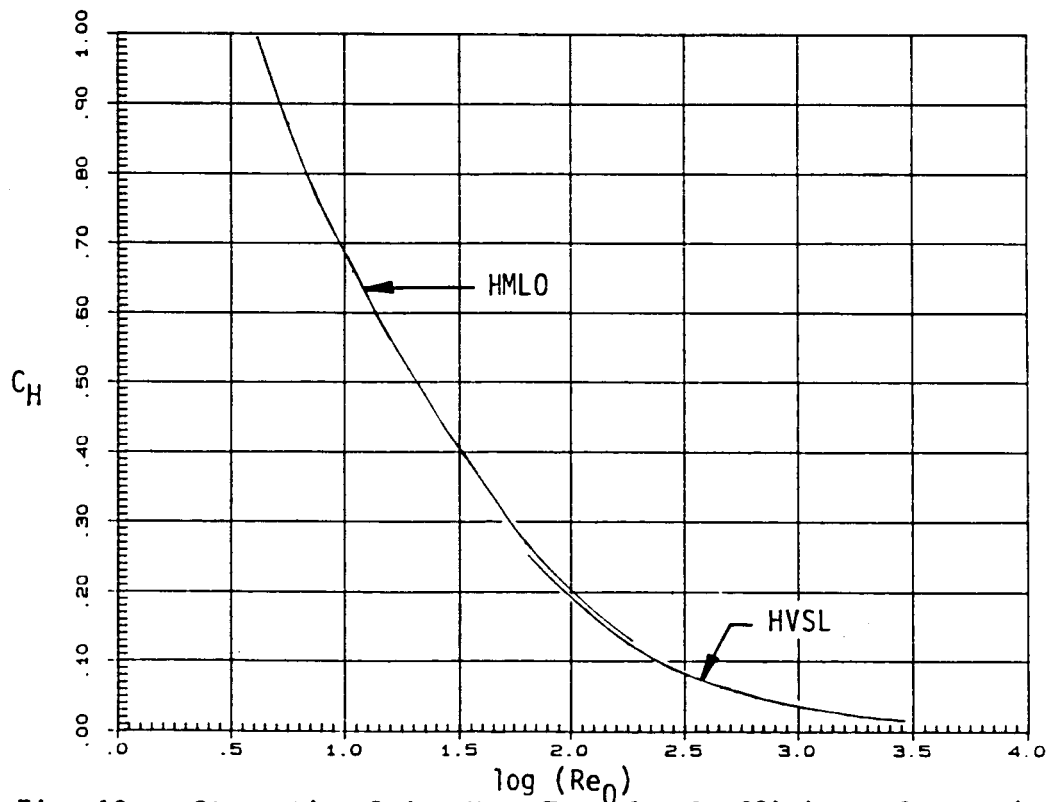   t = 10,20,30 and 40 Seconds of the AFE Trajectory

Fig. 19   Stagnation Point Heat Transfer Coefficient, C_H, against
           log (Reo) from HMLO and HVSL Codes, using Sutherland and
           Square-Root Viscosity Laws along Points on the AFE Trajectory

the viscous layer of the shockwave. Variation of C_H is plotted against the logarithm of the stagnation Reynolds number and against the logarithm of the freestream Reynolds number in Figs. 19 and 20 respectively. Results for C_H were computed from the HMLO Code with Sutherland and square root viscosity laws up to the time t = 40 seconds of the AFE trajectory and from the HVSL Code with square root viscosity law from the time t = 30 seconds to the time t = 90 seconds of the AFE trajectory. At the time t = 90 seconds, the predicted stagnation point heat flux is at its maximum. From Fig. 19, we found that the predicted heating rates when plotted against $\log(Re_O)$ lay on the same curve irrespective of the viscosity law used in the computations, indicating that Re_O is probably the similarity parameter. From Fig. 20, we found that the points for C_H lay on different curves when plotted against $\log(Re_O)$. The HVSL code succeeded in giving results up to the point on the AFE trajectory where highest heating was supposed to occur, viz., up to 90 seconds of the AFE trajectory. It was found that the results of C_H for the HMLO and the HVSL codes almost overlaped between the period 30 seconds to 40 seconds of the AFE trajectory. Thus, the two codes, viz., HMLO or HVSL, complement each other.

In Figs. 22 to 25, we have plotted the temperature profiles, velocity profiles, and surface quantities such as heat transfer coefficient, C_H, and skin friction coefficient, $C_F/\sin\theta$, for values of γ = 1.3 to 1.6 in steps of 0.1 for the AFE conditions at time t = 10, 20, and 30 seconds using the square-root viscosity
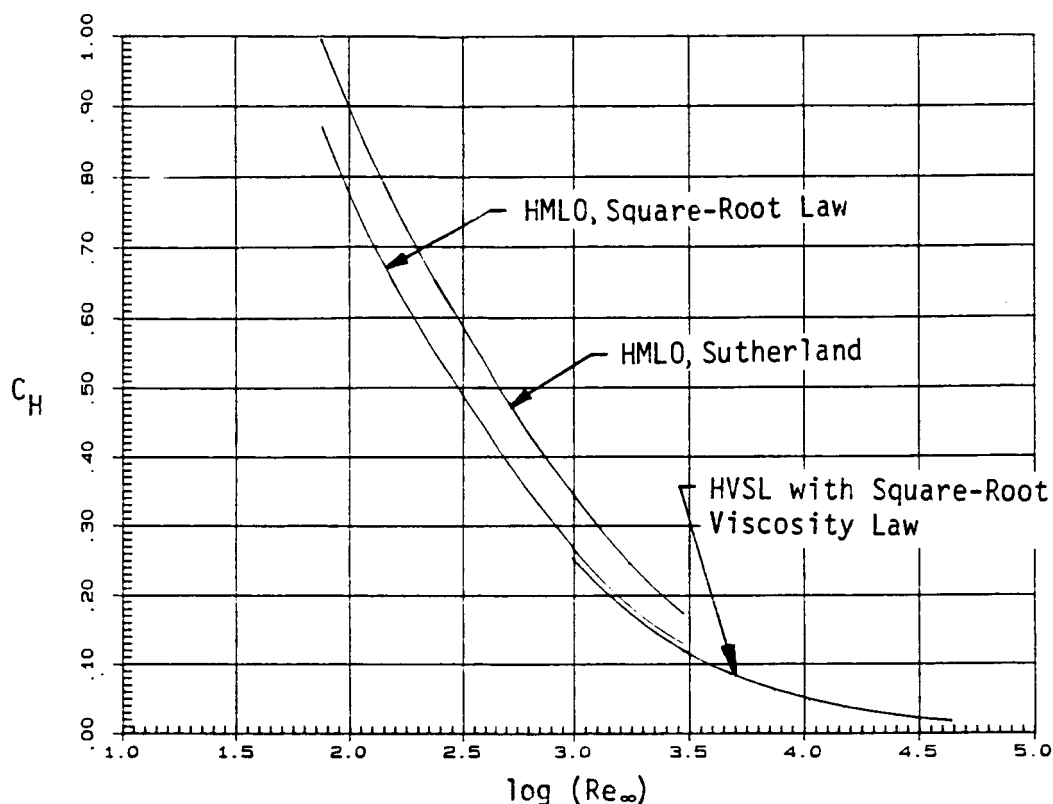
Fig. 20   Stagnation Point Heat Transfer Coefficient, C_H, Against log (Re_∞) from HMLO and HVSL Codes, using Sutherland and Square-Root Viscosity Laws along Points on the AFE Trajectory
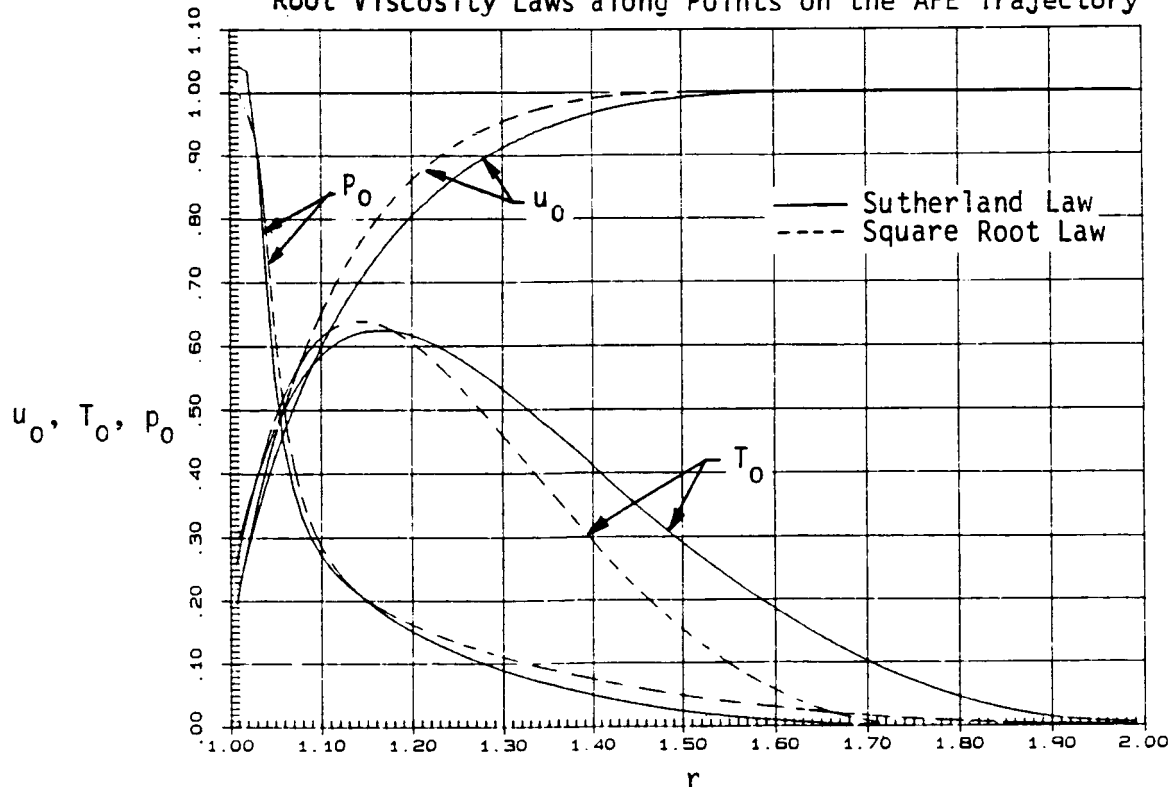

Fig. 21   Comparison of Flow Profiles from HMLO Code using Sutherland and Square-Root Viscosity Laws and at Time t = 10 Seconds of the AFE Trajectory

law. $\gamma = 1.3$ approximates the condition for gases such as freon, used in the NASA Langley tunnel, and also imbibes real gas effects due to vibration and possible dissociation. $\gamma = 1.6$ corresponds to a monatomic gas with translational degrees of freedom only. γ is the ratio of specific heats C_p and C_v. A decrement in γ from 1.6 to 1.3 implies a relatively larger increase in C_v than in C_p. With the increment in C_v the internal energy per unit mass, $e = C_v T$, increases. In other words, the energy required to raise the temperature of a unit mass of the gas 1° will be larger with a greater value of C_v or with a smaller value of γ. Hence, for the given total energy, the temperature level in the ML will be smaller with a smaller value of γ than the temperature level in the ML with a larger value of γ. Fig. 22 showed that as the value of γ decreased, temperature jump at the surface decreased. The maximum temperature inside the ML decreased and the ML thickness decreased significantly. We further observed that the effect of γ was realized more in the outer shockwave-like zone than in the inner viscous layer. With the decrement = γ, the shockwave-like zone becomes thinner and the maximum temperature shifts towards the surface. In Fig. 23, it seems that the trend is reversed. With decrement in γ, ML thickness decreases and the flow is slightly accelerated. This may be due to the fact that with decrease in γ, density across the shock increases while ML thickness decreases. It results in accelerating the fluid faster as it expands downstream of the stagnation line. In Figs. 24 and 25, we have drawn
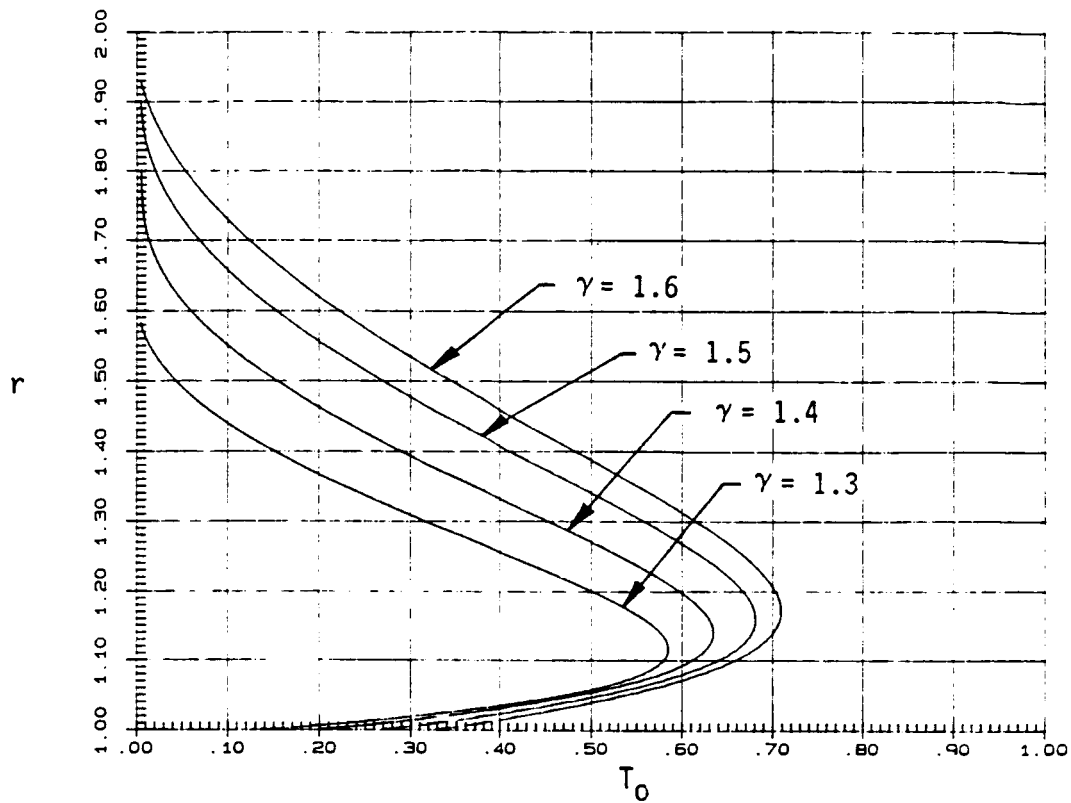
Fig. 22   Stagnation Line Temperature Profiles for γ = 1.3, 1.4, 1.5, 1.6 -
           Pr. No. = 0.72 at Time t = 10 Seconds for the AFE Trajectory

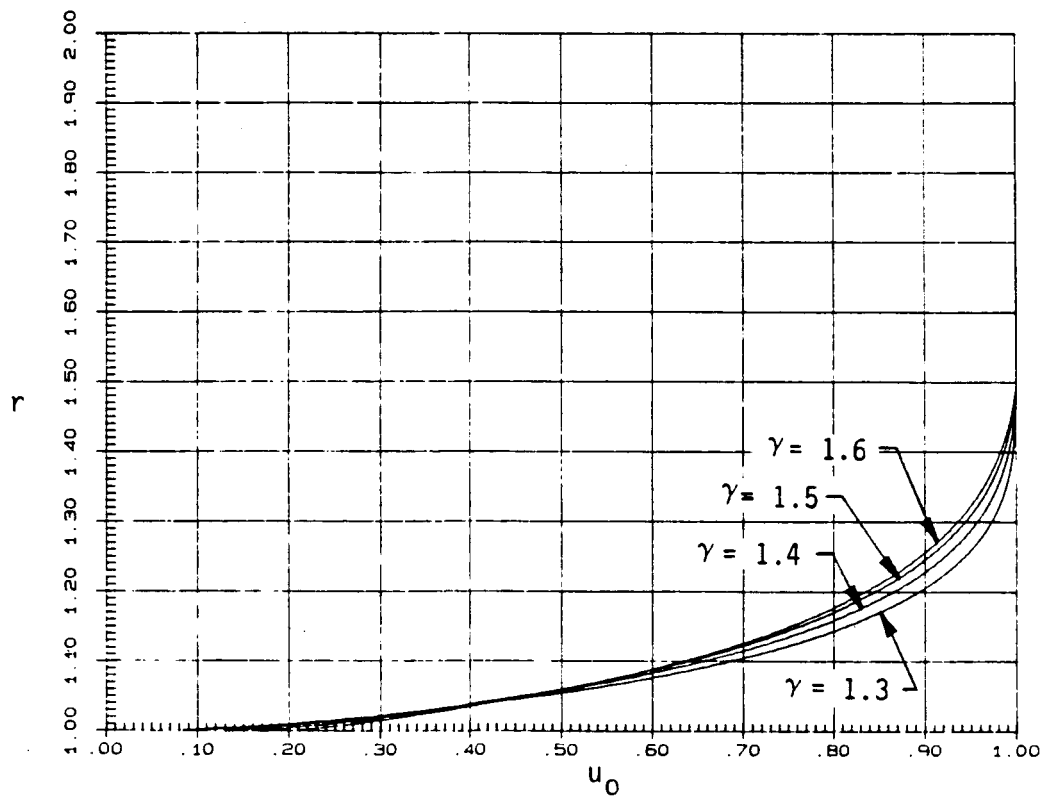Fig. 23   Stagnation Line Velocity Profiles for γ = 1.3, 1.4, 1.5, 1.6 -
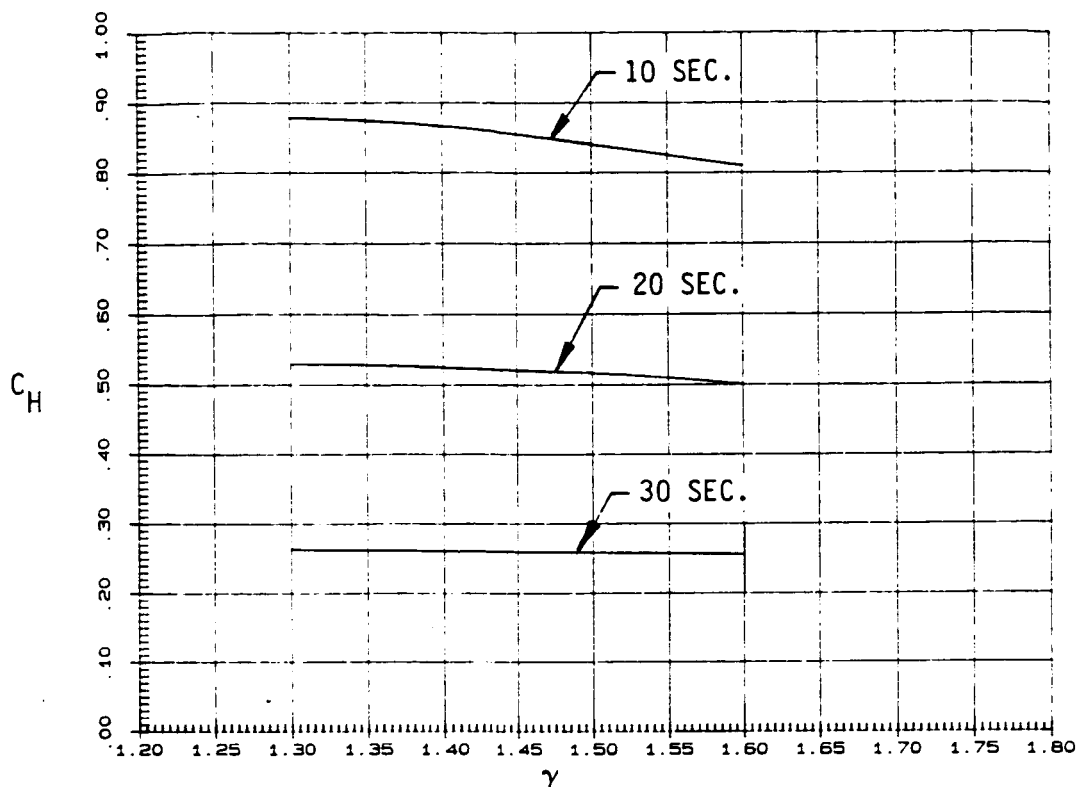   Pr. No. = 0.72 at Time t = 10 Seconds of the AFE Trajectory

Fig. 24   Specific Heat Ratio Effect on Stagnation Point Heat Transfer
Coefficient for t = 10, 20 and 30 Seconds of the AFE Flight
Trajectory

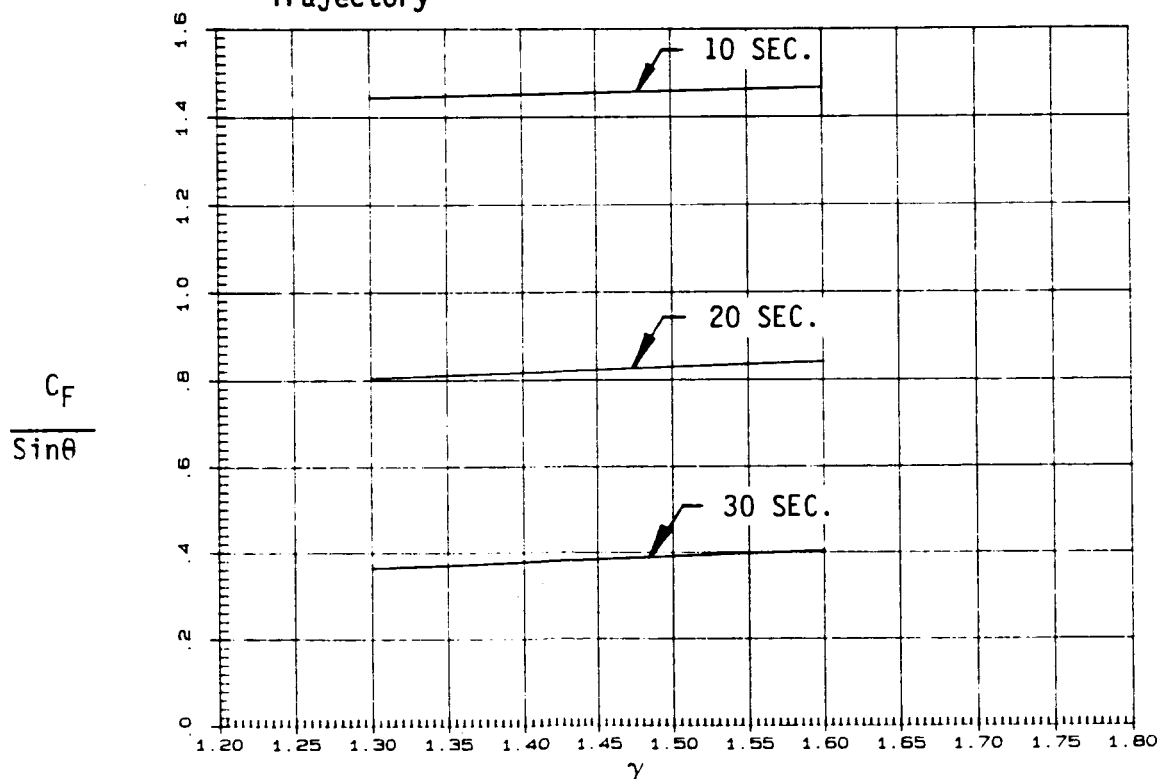

Fig. 25   Specific Heat Ratio Effect on Skin Friction Coefficient for t =
10, 20, and 30 Seconds of the AFE Flight Trajectory

curves for heat transfer coefficient, C_H, and skin friction coeffi-
cient, C_F, for $\gamma = 1.3$ to 1.6 for conditions at times t = 10, 20,
and 30 seconds of the AFE trajectory. We found that the effect of
the variation of γ from 1.3 to 1.6 on C_H and C_F was not signifi-
cant. C_H increased and C_F decreased as γ varied from 1.6 to 1.3.

In Figs. 26 and 27, we have plotted temperature profiles and
heat transfer coefficients, C_H, for values of Prandtl number = 0.6,
0.8, and 1.0. From Fig. 26, we found that as the Prandtl number
decreased, maximum temperature in the ML decreased and the ML
thickness decreased slightly. The decrement in the value of the
Prandtl number implied a value of the thermal conductivity, K,
larger than the value of the product of the viscosity , μ , and the
specific heat, C_p. Thus, whatever heat is generated by dissipation
in the ML is conducted away towards the outer edge of the ML. This
results in the reduction of the maximum temperature inside the
merged layer. Fig. 27 showed an increment of C_H with the decrement
of the Prandtl number. With decrease in Prandtl number, the wall
value of the temperature gradient decreases slightly. However, the
increment in the value of the thermal conductionity, K, results in
the increment of heat flux.

4.3 Real Gas Effects

The HMLORG computer code with slip boundary conditions and ca-
talytic wall conditions was executed for conditions of the AFE tra-
jectory at times t = 10, 15, 20, 25, and 30 seconds. Here, graphs
for t = 30 seconds and 10 seconds are given. We found, from
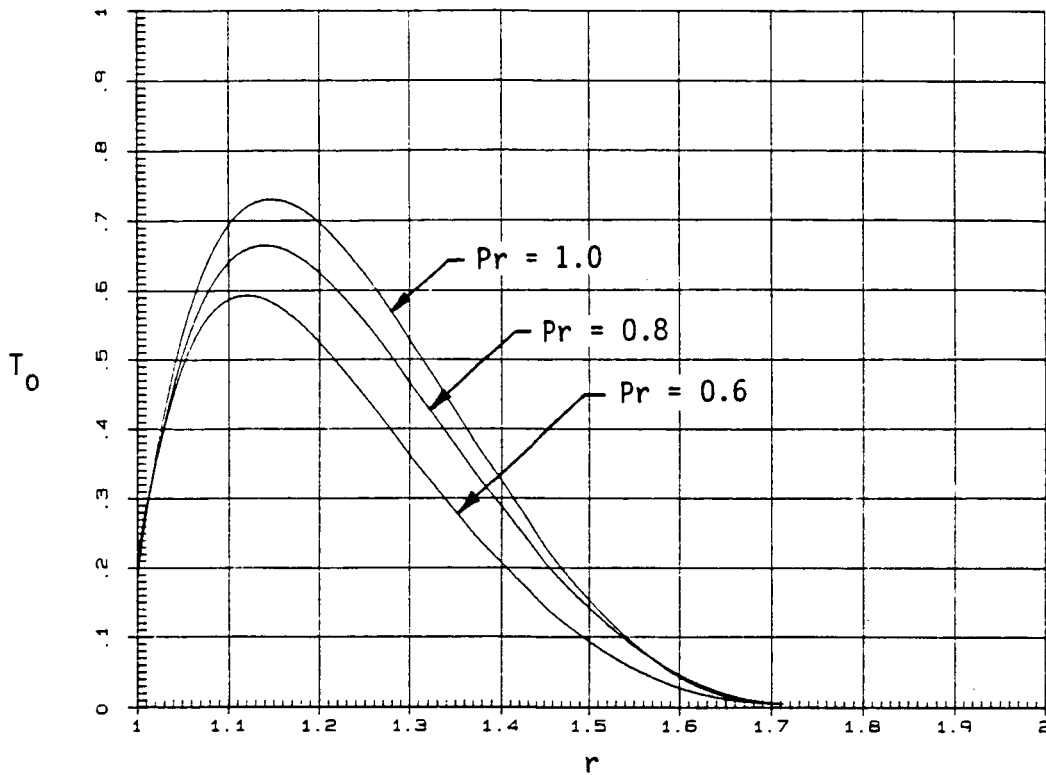
Fig. 26   Stagnation Point Temperature Profiles for Pr. No. = 0.6,0.8,1.0
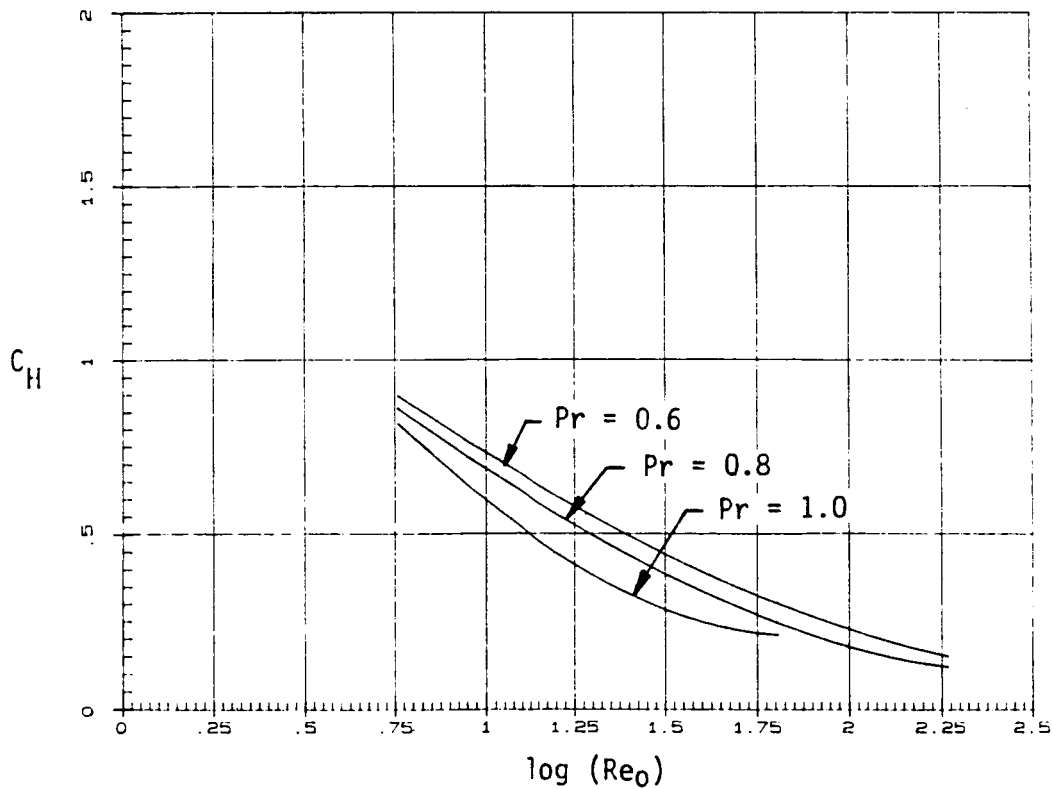and γ = 1.4 at Time t = 10 Seconds of the AFE Trajectory

Fig. 27   Stagnation Point Heat Transfer Coefficient, C_H, for Pr. No. =
0.6, 0.8 1.0 and γ = 1.4 at Time t = 10, 20, and 30 Seconds
of the AFE Trajectory

Fig. 28, that the maximum temperature in the ML was about 40 percent less than its value in the ideal gas ML computations under the same prescribed conditions. (Compare with Fig. 18) This is mainly because the process of dissociation has consumed considerable energy from the flow. Fig. 29 showed that molecular nitrogen is dissociated to about half its value in the freestream and moleculer oxygen is almost completely dissociated at points in the merged layer. There is negligible ionization under these prescribed conditions. Also, due to dissociation and consequent low temperature in the ML, ML thickness is smaller in Figs. 28 and 29 than its counterpart in the ideal gas case (Fig. 18).

In Fig. 30, we have drawn the flow profiles for temperature, tangential velocity component and pressure distributions across the ML for conditions at time t = 10 seconds of the AFE trajectory. In Fig. 31, the corresponding concentration profiles for various species are drawn. From Fig. 31, we found that the flow was almost frozen in the ML and hence, in Fig. 30, the maximum temperature was slightly effected in comparison to the values in the ideal gas case. We thus surmise that as the vehicle descends from the upper region of the atmosphere to the lower region of the atmosphere, the flow characteristics change from the frozen flow to the dissociated and ionized flow.

Fig. 28   Stagnation Point Flow Profiles with Real Gas Effects and Fully Catalytic Wall at Time t = 30 Seconds of the AFE Trajectory

Fig. 29   Stagnation Point Species Concentration Profiles with Fully Catalytic Wall at Time t = 30 Seconds of the AFE Trajectory
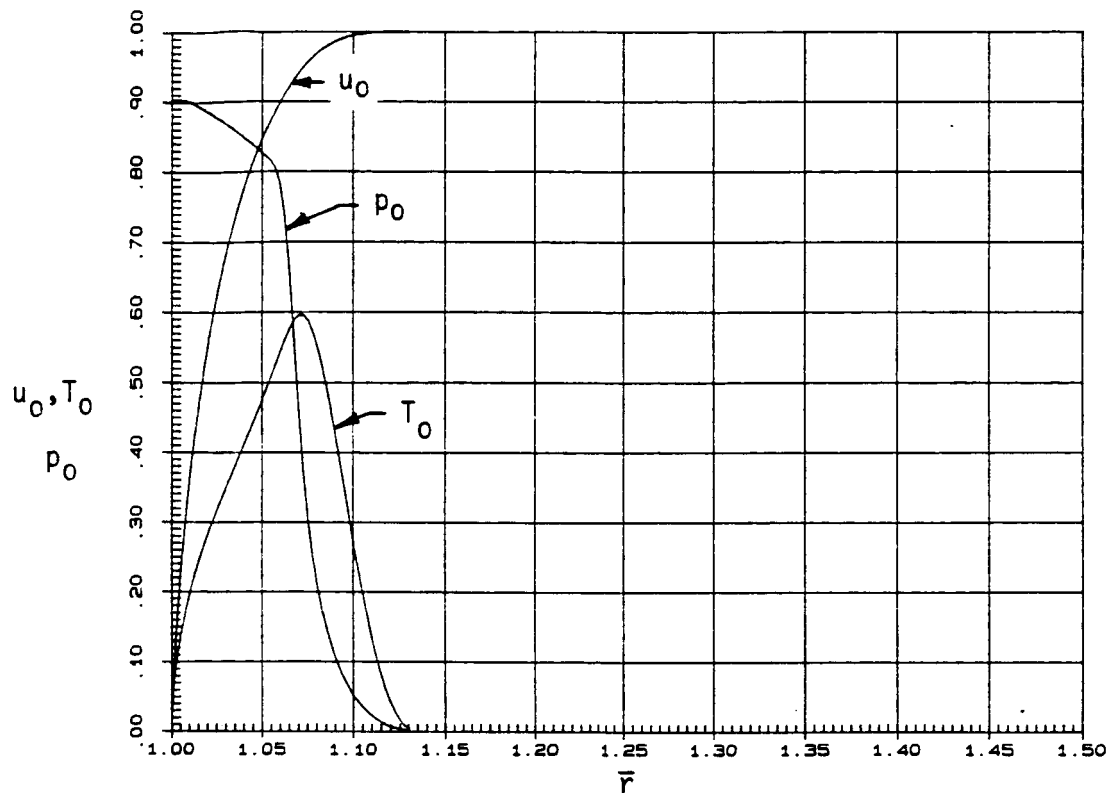
Fig. 30   Stagnation Point Flow Profiles with Real Gas Effects and Fully
           Catalytic Wall at Time t = 10 Seconds of the AFE Trajectory

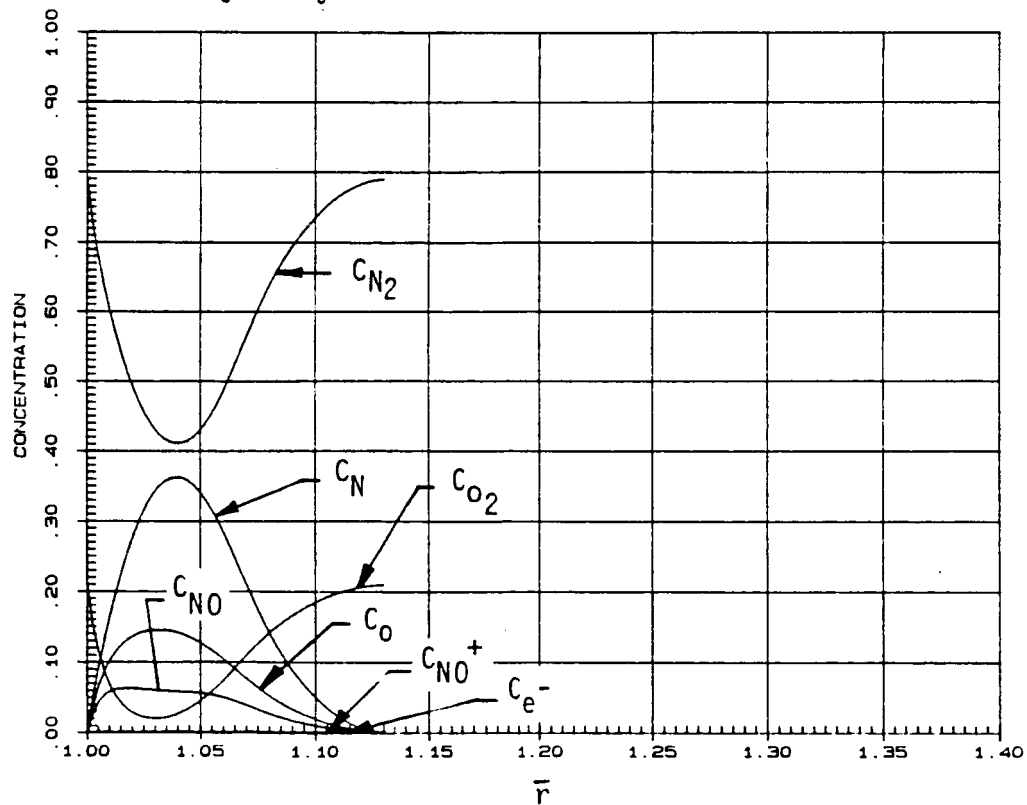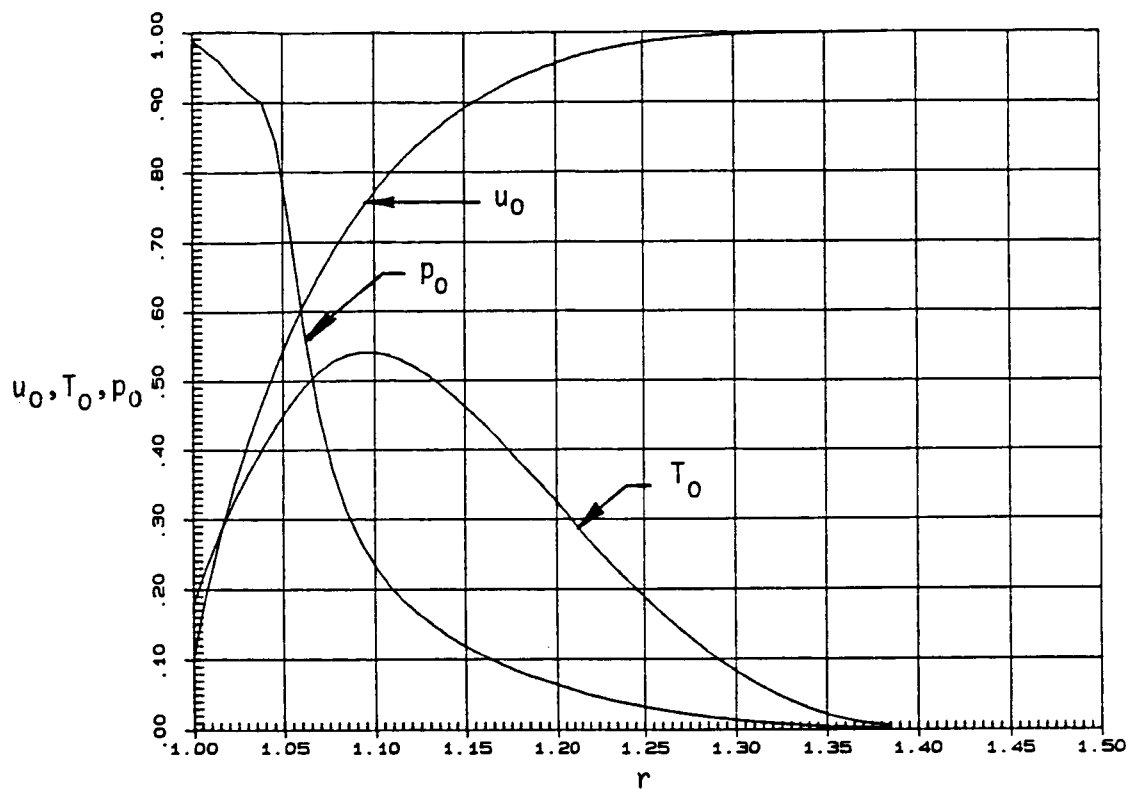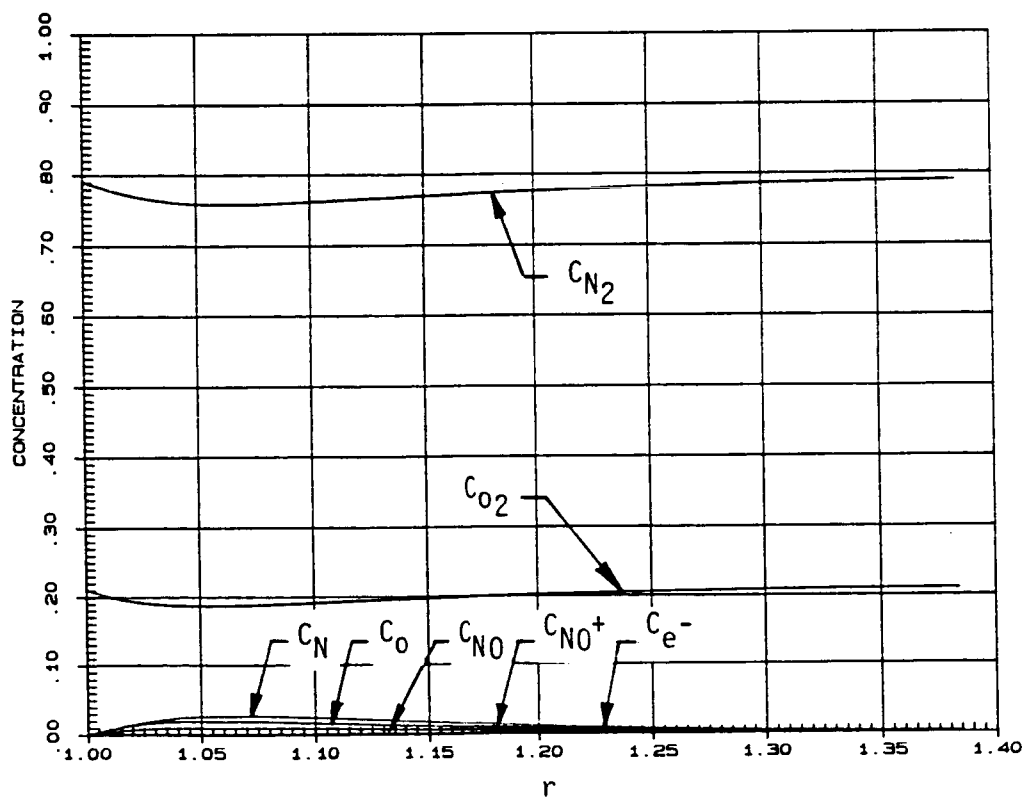

Fig. 31   Stagnation Point Species Concentration Profiles Gas with Fully
           Catalytic Wall at Time t = 10 Seconds of the AFE Trajectory

- 56 -

5.0 TECHNICAL CONCLUSIONS

In order to improve the present solution of the full NS equations on the forepart of the spherical nose of the AOTV and to make the method of numerical integration versatile or robust, we need to incorporate in the analysis the following suggestions.

5.1 Update the Stagnation Line Solution

In the present investigation, the local similar solution of the NS equations gives the stagnation line solution which is held fixed as the iterations of the full NS equation proceed. Due to the elliptic nature of the governing equations, disturbances arising from the downstream position of the fluid should propagate upstream and ought to modify the stagnation line solution. We need to incorporate in the analysis a proper mechanism to account for these down stream effects.

5.2 Develop an Adaptive Grid Generation Technique in the ASR Method of Integration

Gradients in the temperature profiles near the wall and at the interface of the viscous layer and shockwave-like zones are large in comparison to the value of the gradients at any other point in the flowfield. Most of the numerical schemes burst due to inadequacy of the grid points in these regions. Since the location of the maximum gradient point at the interface of the viscous layer and shockwave-like zones is not known a priori, an adaptive grid gereration technique will be suitable for our purpose. In this

scheme, grids automatically cluster around the region where gradients are large.

5.3 Improve Estimates of the Normal Component of Velocity

As suggested in the text, the density profile is evaluated from the continuity equations which become singular at the wall. This singularity is circumvented by imposing certain restrictive conditions on the normal component of velocity near the wall. However, oscillations in the density profile near the wall persist, which affect the pressure profile. There is a need to improve the estimate of the normal velocity near the wall so as to remove oscillations from the density and pressure profiles.

5.4 Incorporate Real Gas Effects

The case for incorporating the real gas effects in the analysis is made from the stagnation point real gas solution, where it is shown that the fluid characteristics change from frozen flow to a dissociated and ionized flow as the vehicle descends from 114 km to about 100 km in altitude. Slip conditions in the presence of real gas effects have already been derived in a form ready for use in computation. There is a need to carry out the complete analysis of the flowfield on the forepart of the spherical nose with real gas effects.

5.5 Develop Capability to Predict Near Wake Structure

The results of the present investigation will provide boundary conditions at surface angle $\theta = 90^\circ$ for investigating the near wake

structure of the flowfield for $\theta > 90°$ (see Phase II proposal). The ASR numerical method used here holds good promise to integrate the NS equations in the near wake flowfield of a body and give reliable estimates for the quantities of a scientific and engineering interest.

If the above suggestions are incorporated in the computer code, we shall be able to solve the flow problem on the forepart and aft body of the spherical nose of the AOTV or AFE up to a much lower altitude of the AFE trajectory.

6.0 TECHNICAL OBJECTIVES AND APPROACH FOR PHASE II

6.1 Significance of the Problem

The Aero-assisted Orbital Transfer Vehicle (AOTV) is supposed to fly from the low earth orbit of the shuttle to geosynchronous orbit, retrieve the satellite, and return to the shuttle after achieving the desired deceleration through grazing the upper region of the atmosphere. In this mission, a novel concept will be used. Air resistance will be utilized to achieve the reduction of its velocity, perform synergetic plane changes and other aerodynamic maneuvers. This concept will reduce the requirements of propulsive material and thus increase the capability for carrying larger pay-loads. However, it demands stringent requirements to develop the capability of predicting accurately the aerodynamic characteristics of the space vehicle.

The reentry velocity of the AOTV will be significantly higher than the reentry velocity of the other space vehicles, such as the Space Shuttle, and the aerodynamic maneuver will take place in the upper rarefied region of the atmosphere. The low density, high energy viscous layer for the forebody of the vehicle may impinge on the payload bay of the vehicle, thus damaging its structure. Even if the afterbody is immersed in the recirculating zone of the wake, it is necessary to assess the thermal environment so as to quantify the thermal protection system. Also, for the success of the mis-sion, we must be able to calculate correctly the aerodynamic forces

(pitching/yawing moments) in the base region and estimate the altitude and the trajectory of the vehicle.

In the area of low density flow with complex chemistry, theoretical investigations and experimental data are very meager. In Sec. 6.1.3, a brief review of the relevant literature is given. It indicated that in the low density area, few theoretical investigations are available and their results are not reliable. They are mostly for the supersonic flow regime. The experimental data are essentially for ideal gas supersonic flow with moderately low Reynolds numbers. Not much is available for predicting the base flow region under hypersonic rarefied conditions. Certain basic questions that are important for understanding the physics of the flow and thus develop a proper design of the afterbody of the vehicle have not been dealt with in the literature. NASA has designed the Aero-assist Flight Experiment (AFE) vehicle which will supply a most comprehensive data base of the flow properties and the surface characteristics. The data so gathered will be used for the development of the AOTV.

6.1.1 Innovation of the Research

Theoretical investigations play an important role in proper interpretation of the experimental data that the AFE is supposed to gather. Flowfield investigations in support of the AFE have been approached mainly in two ways. From the kinetic theory approach, calculations have been carried out on simple bodies using the Direct Simulation Monte-Carlo (DSMC) technique. This approach is

essentially based on binary collisions and consumes considerable computer time for each set of prescribed conditions. It is not clear whether it can compute the recirculating wake flow region of a body correctly. The other way to tackle the problem is based on a continuum approach using the full Navier-Stokes equations with proper modeling of the flowfield. In Sec. 6.1.2, the present status of the capability of the continuum approach to solve the hypersonic rarefied flow problem is given. With a view to develop proper modeling of the flowfield under hypersonic rarefied conditions, to develop numerical techniques capable of predicting separation and reattachment of the flowfield, and to understand the basic physics of the flow, initially a simple shape body such as a sphere is selected for further investigation. The mathematical formulation adopted here has the capability to calculate the flowfield on bodies of arbitrary shape such as an AFE. In the SBIR Phase I, it has been demonstrated that the Merged Layer (ML) model of flow with surface slip boundary conditions together with the Accelerated Successive Replacement (ASR) numerical scheme of integration has the capability to simulate the flowfield on the forepart of the spherical surface under hypersonic rarefied conditions. A number of graphs are drawn to illustrate the salient features of the flowfield and provide vital information about surface quantities under conditions that the AFE will encounter at times t = 15 seconds and 20 seconds of its early entry phase. For lack of time and resources, it was not possible to develop data for more points

of the trajectory and improve upon the numerical method of integra-
tion to make it versatile and robust. In the SBIR Phase II effort,
we first intend to incorporate certain improvements in the
mathematical formulation of the flowfield on the forepart of the
sphere so as to make the computations capable of predicting the
flowfield in the denser region of the AFE trajectory. Then, use
the results so obtained will be used to provide boundary conditions
for calculating the flowfield in the near wake region of the
sphere. In the literature it has been established that the
forepart flowfield is weakly dependent upon the aftbody flowfield.
As such, it is expected that the results of the Phase I will pro-
vide reasonably accurate boundary conditions for integrating the
full Navier-Stokes equations in the near wake region of the flow-
field. The technical approach to the SBIR Phase II problem is
given in Sec. 6.2. It is hoped that the present approach will, for
the first time, enable us to understand the rarefaction effects on
the structure of the near wake region. The mathematical approach
adopted here has the potential to include nonequilibrium ionization
and radiation effects and to extend to bodies of arbitrary shape.

6.1.2 **Validity of Continuum Approach in the Transitional Regime**

In the present investigation, it is proposed to investigate
the flowfield on the entire surface of the space vehicle through
the continuum approach based on the full steady-state Navier-Stokes
(NS) equations. Several investigations have questioned the
validity of the continuum approach for investigating the rarefied

regime that a vehicle encounters during its reentry period. The present author (ACJ) has been investigating this regime for the last fifteen years. In Refs. 6 and 7, Jain and Adimurthy made a detailed comparison of their computations of stagnation point flow with the experimental data for temperature profiles of Ahouse and Bogdonoff (20), for density profiles from Russell (21), and for surface pressure distribution of Potter and Bailey (19). It was found that the validity of the Navier-Stokes equations can be extended to surprisingly low Reynolds numbers. In Ref. 13, further comparison with the Direct Simulation Monte-Carlo Technique (DSMC) showed that the Navier-Stokes equations can predict accurate results up to Knudsen No. = 0.6. In Ref. 9, it was found that the current results based on the NS equations compare reasonably well with the DSMC results for the shuttle flight trajectory up to an altitude of 110.4 km. Gupta (26) improved upon the fluid property description of the formulae of Kumar and Jain (22) and Henricks (14) and found that the results can be extended up to an altitude of 115 km of the shuttle flight trajectory. There is some controversy in the prediction of the structure of the outer shockwave-like region in the continuum and the kinetic approaches, but the surface quantities and the flow structure near the surface from the predictions of the two approaches agree reasonably well. It is difficult to give a mathematically rigorous proof of the validity of the Navier-Stokes equations in the hypersonic rarefied regime. However, based upon the detailed comparison of the results

from the NS equation with the experimental data and DSMC calcula-
tions, we may surmise that the validity of the NS equations can be
extended well beyond the theoretically permissible limits.

6.1.3 Relevant Literature

From the literature survey, we found that most of the in-
vestigations of the flowfield on a complete body under low density
conditions had been for low supersonic conditions. In Ref. 29,
Pavlov solved the unsteady Navier-Stokes equations with no slip
boundary conditions on a thermally insulated body of elliptic shape
for $M_\infty = 2.0$ and $Re_\infty = 90$. Pavlov found weak dependence of the
flow on the forepart of the body on the flow in the rear part of
the body which permits the calculations on the fore and aft part of
the body separately without losing accuracy. We observed from his
graphs that there was no separation of the flowfield under the pre-
scribed conditions. In Ref. 30, Kitchens investigated the flow on
a cylinder by solving the unsteady-state Navier-Stokes equations
with no slip boundary conditions for $M_\infty = 2.0$ and Reynolds number
based upon the cylinder diameter, Re_D, varying from 15 to 705. He
found that at $Re_D = 157.2$, a small separation bubble with separa-
tion starting at surface angle $\theta = 158^\circ$ appears. In Ref. 31, Tassa
and Conti investigated the flow on a conical body with a flat base
by solving the NS equations with no slip and adiabatic wall condi-
tions for $M_\infty = 4.32$, 6.32 and 10.0 and Re_D varying from 21,500 to
172,000. They found that the length of the separation bubble
depended greatly on both the Mach number and Reynolds number. At

M_∞ = 6.32 and Re_D = 86,000, the separation started from a point in the base region below the corner. This indicated the possibility that the separation point may shift further towards the center of the base as the Reynolds number decreases.

In Ref. 32, Gnoffo solved the NS equations on the AFE vehicle, simplified by removing protuberances and adding certain solid surfaces to make it amenable to mathematical description. He obtained numerical solutions at the maximum dynamic pressure point of the AFE trajectory with V_∞ = 8.917 km/sec and Re_∞ = 79 x 10^3 and 2.86 x 10^6 and presented graphs for the detailed structure of the flow. He did not obtain a fully converged solution for the complete flow-field. However, he found the flow impingement of the shear layer on the nozzle tip where the local heating shoots up much above the stagnation point value.

In Ref. 33, Dogra, Moss and Simmonds calculated the flowfield on the forepart of the AFE vehicle at zero angle of attack using the kinetic approach based upon Direct Simulation Monte-Carlo Technique (DSMC) with chemical reactions under conditions that the AFE will fly from 130 km to 90 km. A number of graphs are drawn to illustrate the flowfield and the surface quantities. Wherever possible, they indicated the effect of rarefaction on the surface quantities. Bird (34), using the DSMC technique, calculated the effect of nonequilbrium radiation on the flowfield at a reentry velocity of 10 km/sec of a space vehicle while Park (35) solved a similar problem using a continuum approach. Jones (36) pointed out

the importance of correctly estimating the thermal environment in the base region of the AFE vehicle.

In Ref. 37, Krylov, Banov, and Starikov have measured normal and tangential stresses for Re_D varying from 31.6 to 520 and Mach number less than 6. Using a specially designed floating element technique, they found negative values of the tangential stresses indicating separaton at the surface angle $\theta = 110^{\circ}$. Allegre, Raffin and Vennemann (38) measured the axial velocity in the near wake of a cone for $Re_D = 2200$ and $M_{\bullet} = 4$ to 20 and by a direct measurement technique called the Ion Time-of-Flight technique and found that the axial velocity increases with the increase of Mach number. Koppenwallner (39) measured the surface pressure distribution on the surface of cylinder with Reynolds number based on the conditions behind the shock varying from 25.9 to 79.8 and Mach No. =23. If the pressure minimum represents the separation point, we found that the separation point shifted towards the axis of the cylinder as the rarefaction of the fluid increases.

Most of these experimental set-ups suffered from probe interference or tunnel interference or from both. Blankson and Morton (40) overcame the support interference problem by measuring the near wake of a magnetically suspended cone by pitot probe. However, Crane (41) pointed out that these experimental results suffered from probe interference.

From the review of the relevant literature, we suggest the intuitively derived fact that with the increase in rarefaction or

decrease in Reynolds number the separation point shifts towards the rear axis of the blunt body and the rear stagnation point moves towards the base of the body. In other words, the recirculating zone or the separation bubble shrinks in extent as the Reynolds number decreases.   The effect of increasing the Mach number is similar to the effect of decreasing the Reynolds number.

6.1.4 Specific Objectives

The research performed during Phase II will be directed toward two main objectives. These objectives are that the forebody solution be improved to provide boundary conditions for the wake flow and that the near wake solution of flow around a sphere be investigated using the Navier-Stokes equations.

The range of validity for the forebody solution will be extended by incorporating a grid generation mechanism that stretches or shrinks the grid size according to the flow variable gradients. The oscillations observed in the forebody solution will be removed by accounting for the downstream effects at the stagnation line.

In order to apply the Navier-Stokes equations to the near wake flow problem, suitable transformation of the independent variables will be chosen. Also, in order to study the recirculating flow region, a numerical scheme of second order accuracy will be selected. The near wake flow structure will be analyzed.
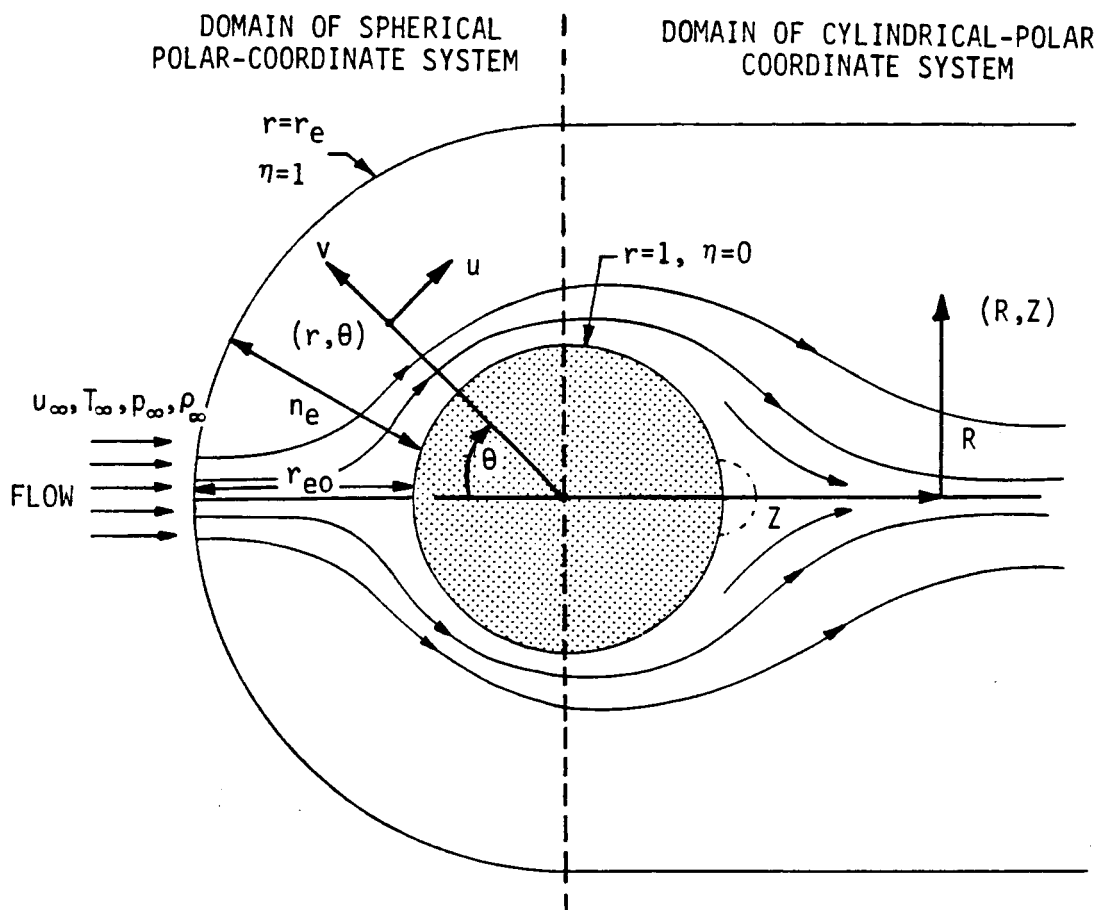
6.2 Technical Approach
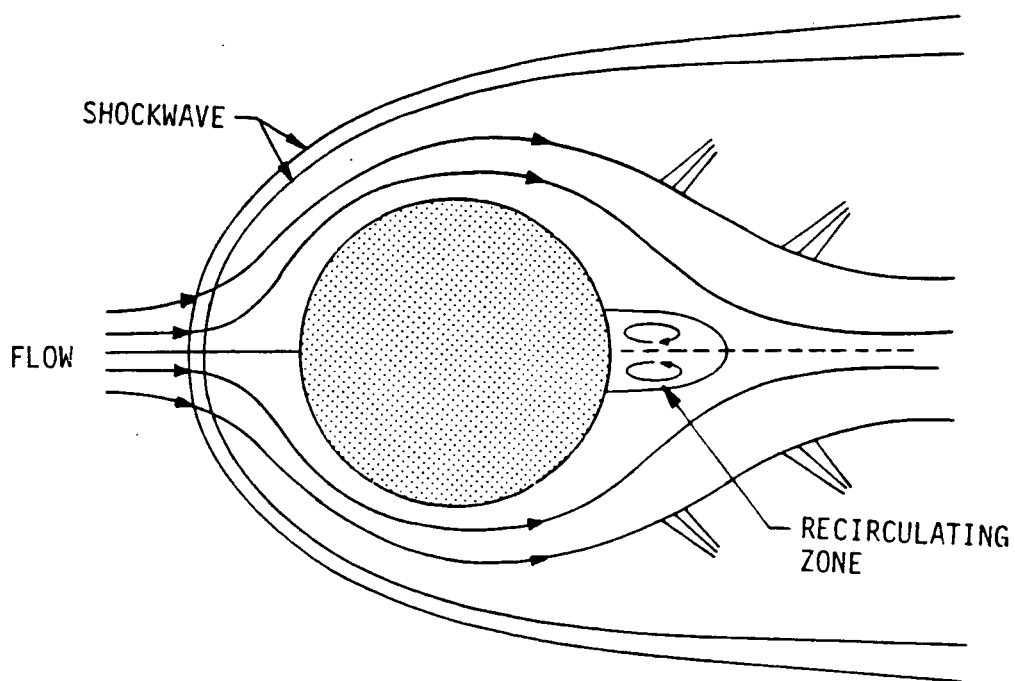
6.2.1 Physical Modeling of the Problem

The objectives of the SBIR Phase II proposal are to compute the near wake flowfield of a spherical body under hypersonic rarefied conditions and provide a good understanding of the rarefaction effects on the aerodynamic coefficients and the aerothermal environment in the aft portion of the body.

In the aft part of the vehicle flowfield, rarefaction effects are manifested. As the vehicle descends to the denser region and continuum flow develops, an adverse pressure gradient in the aft portion is generated which tends to decelerate the fluid between two streamlines and increase the distance between them. With further increase in the ambient density, a separation bubble develops from the rear axis on the sphere. A schematic representation of this pattern of the flow is given in Fig. 32a.

The initial stage of the wake development is highly sensitive to both the variation of Mach number and Reynolds number. The mean free path is proportional to (M_∞ /Re_∞). Therefore, increasing the Mach number or decreasing the Reynolds number will increase the rarefaction effects in the flowfield. In the transitional regime, it was found (38, 39) that increasing the Mach number shifts the separation point towards the rear axis of the sphere and moves the rear stagnation point towards the surface. In other words, the effect of increasing the Mach number is to diminish the extent of the separation bubble. A similar pattern emerges from decreasing the

DOMAIN OF SPHERICAL
POLAR-COORDINATE SYSTEM

DOMAIN OF CYLINDRICAL-POLAR
COORDINATE SYSTEM

$r=r_e$

$\eta=1$

$r=1, \eta=0$

(R,Z)

v

u

(r,θ)

$U_\infty, T_\infty, p_\infty, \rho_\infty$

n_e

R

FLOW

θ

r_{eo}

Z

(a) Low Reynolds Number Flow

SHOCKWAVE

FLOW

RECIRCULATING
ZONE

(b) High Reynolds Number Flow

Fig. 32   Hypersonic Near Wake Flow

Reynolds number. An opposite trend in the flow pattern is observed
with increasing the Reynolds number. The separation point moves
upward up to a certain value of the Reynolds number and then it be-
comes independent of the Reynolds number. The rear stagnation
point moves away from the spherical surface, thus increasing the
extent of the recirculating zone. Compression shocks, separation
shocks, etc., may be formed in the wake flow region. A schematic
representation of the pattern of the near wake flow at a moderately
high Reynolds number is given in Fig. 32b. The main purpose of
this investigation is to understand the development of the near
wake region as the vehicle descends from the upper rarefied regime
to the lower denser regime and study the phenomena associated with
the near wake closure and viscous layer impingement at the neck of
the wake. Aerodynamic coefficients such as pitching and yawing
will be derived and the thermal environment will be studied.

With a view to study the physics of the flowfield associated
with the various phenomena in the near wake and to develop a method
of solving the full Navier-Stokes equations in the aft portion, we
intend to study the flow on a simple body such as a sphere.
However, the present formulation can be extended to solve the flow
problem on bodies of complicated shapes and to include real gas ef-
fects.

6.2.2 Mathematical Modeling of the Flowfield

The present attempt to solve the aft flow near wake problem
under hypersonic rarefied conditions is the result of the

cummulative efforts that the present author (ACJ) along with his
co-workers has been pursuing for the last fifteen years. These ef-
forts are directed upon the proper modeling of the flowfield
through the continuum approach based upon solving the full
steady-state Navier-Stokes equations under various prescribed con-
ditions. Here, a modular approach to solve the complete flow
problem on a body is adopted. In module one, the stagnation point
merged layer (ML) flow problem (6,7) was solved through the local
similar solutions of the full Navier-Stokes (NS) equations using
surface slip and temperature jump boundary conditions. The govern-
ing equations were integrated from the surface to the free stream
so that the shockwave-like structure was computed as part of the
solution. The accuracy of the results was demonstrated through
comprehensive comparison with experimental data (6) and with the
Direct Simulation Monte-Carlo (DSMC) results (13). In Refs. 9 and
22, the method was extended to nonsimilar solutions to analyze
downstream effects on the stagnation line and to include real gas
effects. In module two, the stagnation line solution provided one
of the boundary conditions to the solution of the full
Navier-Stokes equations for solving ML flow on the forepart of the
spherical surface. We obtained reasonably good results for flow
conditions that the AFE vehicle will encounter at times t = 15
seconds and 20 seconds of its flight trajectory. This formed the
subject matter of the SBIR Phase I proposal. In module three, the
results of module two will provide boundary conditions to the

solutions of the full Navier-Stokes equations for studying the near wake structure on the rear part of the spherical surface under conditions that the AFE will encounter in its entry to the upper atmosphere.   It is surmised in Section 6.1.1 that the forepart flow will provide reasonably accurate boundary conditions for the solution on the rear part of the spherical surface.

In Fig. 33, the domain of integration consists of line 1 at surface angle $\theta = 90^\circ$ (outermost boundary of the domain of integration on the forepart of the spherical surface), the rear part 2 of the spherical surface ($90^\circ < \theta < 180^\circ$), the axis of symmetry 3 ($\theta = 180^\circ$), the outer flow boundary 4 sufficiently far off where the flow becomes supersonic and the outermost boundary 5 where freestream conditions are realized.   On line 1, the dynamic and thermodynamic variables are given by the solution in the forepart of the sphere. On line 2, surface slip and temperature jump boundary conditions will be used. On line 3, symmetry conditions will be employed. On line 4, linear quadratic extrapolation of the flow variables will reasonably well represent the physical situation. In view of the supersonic nature of the flow on line 4, it is expected that the disturbances due to some inaccuracy in this boundary condition will not propagate upstream and vitiate the solutions. On line 5, prescribed uniform flow exists.

The flow on the forepart of the spherical surface was calculated using a spherical polar coordinate system and uniform grids within a finite domain of integration. If we continue to use the
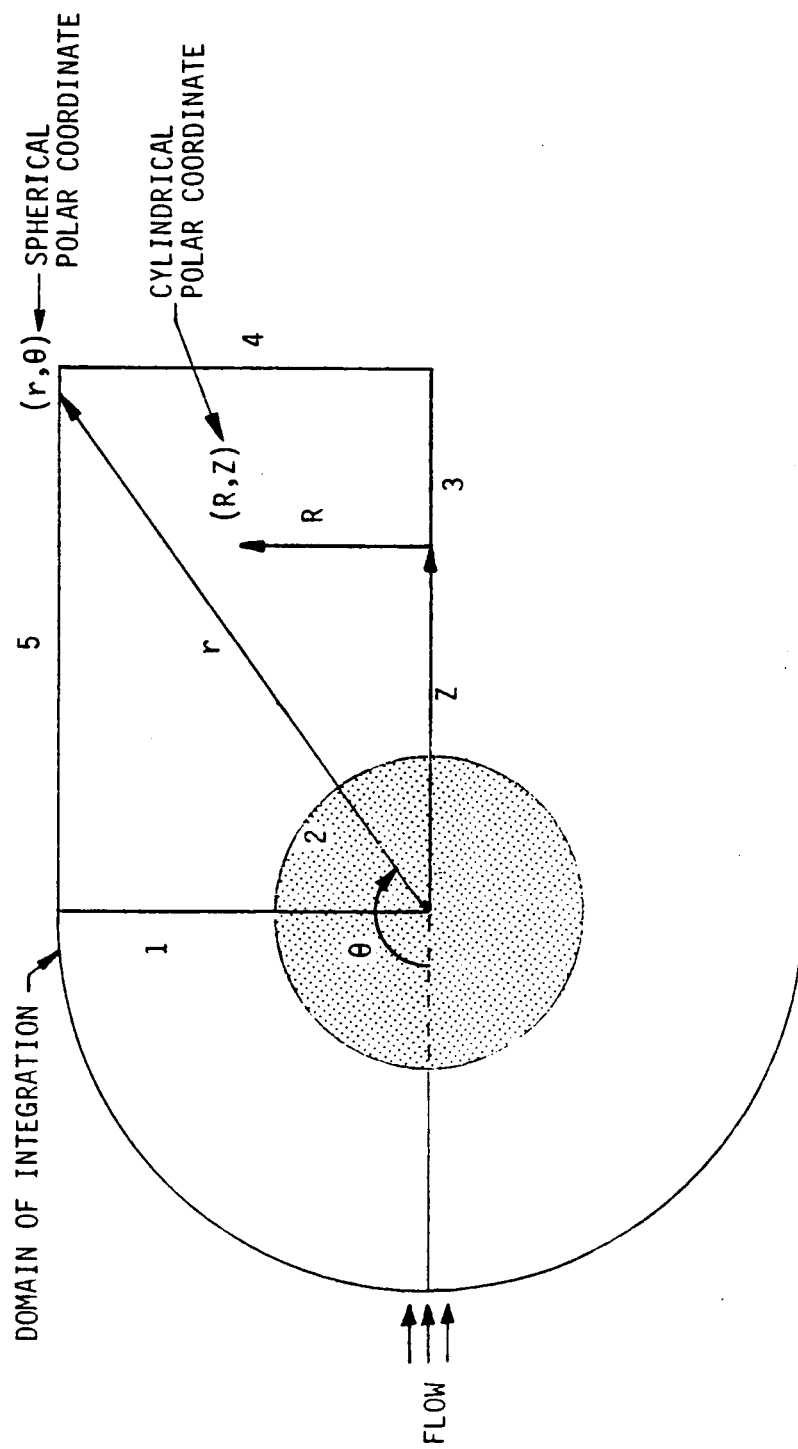
Fig. 33   Domain of Integration for Near Wake Flow

same coordinate system in solving the NS equations for the rear part flowfield, a radial line lying between $90^\circ < \theta < 180^\circ$ will meet the outer boundary of integrations at a far distance making the grid size coarse enough that it will either burst the numerical scheme of integration or fail to catch the finer characteristics of the flow. In order to avoid this problem, we intend to use the cylindrical polar coordinate system in the domain of integration defined by $90^\circ < \theta < 180^\circ$ with the z-coordinate along the axis of symmetry and the radial coordinate, r, perpendicular to it. In this manner, we can maintain uniform grids throughout the rear part of the flowfield and get fine resolution of the flow structure. The QUICK computer code developed at NASA Langley Research Center also uses the spherical-cylindrical coordinate system, and accomodates complicated geometry like the Shuttle. In view of the availability of the QUICK computer code, it should be possible for us to extend our computations of the NS equations to investigate the flowfield on bodies of arbitrary shape.

The numerical scheme of integration should be able to catch recirculating flow that may possibly exist in the rear part of the flowfield of the sphere. In a recirculating flow, the velocity changes both in magnitude and direction as one moves along a line perpendicular to the axis. We need to develop a finite-difference approximation of the convective terms in the NS equations that change sign with the change in direction of the velocity in the flowfield. The present investigator (ACJ) (42) used a second order

upwind finite-difference scheme of integrating the NS equations for investigating the structure of trailing vortices of an aircraft and succeeded in catching the recirculating zone in the bubble of the trailing vortex. It is suggested that a similar scheme for compressible flows be used for integration purposes. A review of the presently available upwind finite-difference schemes will be undertaken. The numerical scheme that is capable of catching the recirculating flow with posible shocks will be selected for putting the governing partial differential equations to finite-difference equations which together with the boundary conditions will be solved by the Accelerated Successive Replacement (ASR) technique.

7.0 STATEMENT OF WORK

The feasibility of solving the Navier-Stokes equations to in-
vestigate hypersonic rarefied flow around a blunt body was deter-
mined during Phase I. The research effort of Phase II will attempt
to improve the flowfield quantities in the narrow stagnation zone
on the forebody and to model the near wake flow structure on the
rear part of a sphere. At the conclusion of the Phase II in-
vestigation, REMTECH will deliver a set of computer codes that can
be used to predict flow quantities in the entire flowfield, includ-
ing the forebody and afterbody solution, for the AFE trajectory.
The specific tasks to be performed in order to meet these objec-
tives are outlined below.

**Task 1 Incorporation of Downstream Effects on the Stagnation
Line Solution**

The importance of updating the stagnation line solution with
downstream effects has been pointed out in the text. We may update
the stagnation line solution in several ways. A few of them are
listed below:

(i) Approximate the NS equation along the stagnation line us-
ing symmetry conditions and use the resulting equations
along with the full NS equation for calculating the flow-
field.

(ii) Use the symmetry conditions in the differential form such
as $\frac{\partial v}{\partial \theta} = \frac{\partial T}{\partial \theta} = \frac{\partial p}{\partial \theta} = 0$ etc. to solve the full NS equation.

(iii) Improve the estimate of the normal component velocity by
solving the normal momentum and the continuity equation
iteratively in each global iteration.

(iv) Use a second order accurate three point finite-difference approximation for the first order derivative in the tangential direction up to a few points downstream of the stagnation line.

It is hoped that suggestions like the above will help us to remove oscillations in the surface quantities and in the stagnation zone.

Task 2   Incorporation of Grid-Generation Technique in the Mathematical Analysis

Large gradients in the flow variables occur near the surface and at the interface of the inner viscous layer and the outer shockwave-like layer. Also, the location of the interface is not known a priori. As such, it seems appropriate to try an adaptive grid generation technique, which puts additional grids wherever large gradients occur in the flowfield.

Task 3   Analytical Calculations of the Navier-Stokes Equations

A suitable transformation of the independent variables is to be selected which will transform the physical plane of integration into a simpler computational plane. We then transform the boundary conditions from the various segments of the physical plane to the corresponding segments in the computational plane. The full Navier-Stokes equations in cylindrical coordinates will also be expressed in the coordinate system of the computational plane. With the suggestions given in Task 4, we shall choose a suitable finite-difference scheme and express the transformed partial differential equations governing the flow in finite-difference equation form.

Task 4 **Examination of a Suitable Upwind Finite-Difference Scheme**

A review of the available upwind finite-difference schemes in the literature will be undertaken. A numerical scheme of at least second order accuracy and suitable for computing recirculating flow will be chosen to approximate the first order derivatives in the convective terms of the governing equations. Second order derivatives will be replaced by the usual three point formula.

Task 5 **Develop the Computer Code, Validate and Document**

A computer program to solve the finite-difference equations which govern the flowfield at every grid point in the computational plane will be written and run on the MICRO VAX II computer of REM-TECH, Inc. Efforts will be made to remove all the bugs in the computer program and to reduce computer time and storage requirements. We hope to be able to develop a robust and efficient computer code for investigating the near wake structure. A few experimental data are available for low supersonic and moderately low Reynolds number flow. As stated in the review of literature in Sec. 6.1.3, the data suffer from either support interference or probe intereference or from both. Still the computer code will be tested to see if we can reproduce these data at least qualitatively. The computer code will be documented in the form of a User's manual where statements about the input, output, and the explanation of the various symbols used in the code will be given. Also, test runs will be presented for easy use of the computer code by later investigators.

Individual tasks will be performed simultaneously throughout the two year period of performance as shown in the master schedule of Table 3. Quarterly written and oral progress reports will be delivered/conducted as shown on the schedule. Major milestones and significant events, such as experiment set-up briefings and a final design review, will occur throughout the program and may require separate reports and data transmittal. A final report documenting system design, development and verification, test results, and analysis of results as compared with work by other investigators will be delivered to MSFC at the conclusion of the contract. A copy of the computer codes on magnetic media will also be delivered to MSFC, along with a User's manual explaining the operation of the modeling tool.

Table 3   Hypersonic Rarefied Flow Investigation Task Schedule

TASK	QUARTERS FROM GO-AHEAD							
	1	2	3	4	5	6	7	8
1. Downstream Effects								
2. Grid Generation								
3. Navier-Stokes Calculations								
4. Finite Difference Scheme								
5. Code Development								
6. Code Validation								
7. Documentation and Code Delivery								
8. Quarterly Progress Reports								

REFERENCES

1. Walberg, G.D., "Aeroassisted Orbit Transfer - Window Opens on Missions," Astronautics and Aeronatuics, Vol. 21, Nov., 1983, pp. 36-43.

2. Victoria, K.J. and Windhopf, C.F., "Numerical Solution of the Unsteady Navier-Stokes equations in Curvilinear Coordinates. The Blunt Body Merged Layer Problem," presented at the Third Int. Conf. on Numerical Methods in Fluid Dynamics, Univ. of Paris - Orsay, July 3 - 7, 1972.

3. Li, C.P., "Hypersonic Nonequilibrium Flow Past a Sphere at Low Reynolds Numbers," AIAA Paper No. 74-173, 1974.

4. Dogra, V.K., Moss, J.N. and Simmonds, A.L., "Direct Simulation of Aerothermal Loads for an Aeroassist Flight Experiment Vehicle," AIAA Paper No. 87-1546, 1987.

5. Lieberstein, H.M., A Course in Numerical Analysis, Harper and Row, New York, NY and John Weatherhill, Inc., Tokyo, 1969.

6. Jain, A.C. and Adimurthy, V., "Hypersonic Merged Stagnation Shock Layers, Part I: Adiabatic Wall Case and Part II: Cold Wall Case," AIAA Journal, Vol. 12, No. 3, 1974, pp. 342-354. Also, see AIAA Paper No. 73-639, 1973.

7. Jain, A.C., "A Comparative Study of Steady and Time-Asymptotic Navier-Stokes Equations under Hypersonic Rarefied Conditions," Proc. of the Thirteenth Int. Sym. on Space Technology and Science Tokyo, June 28 - July 3, 1982, pp. 503-508.

8. Bird, G.A., "Aerodynamic Properties of Some Simple Bodies in the Hypersonic Transition Regime," AIAA J., Vol. 4, No. 1, pp. 55-60.

9. Jain, A.C., "Hypersonic Merged Layer Flow on a Sphere," J. Thermophysics and Heat Tranfer, Vol. 1, No. 1, 1987, pp. 21-27.

10. Boylan, D.E., "Laminar Convective Heat Transfer Rates on a Hemisphere-Cylinder in Rarefied Hypersonic Flow," AIAA Journal, Vol. 9, Aug. 1971, pp. 1661-1663.

11. Moss, J.N. and Bird, G.A., "Direct Simulation of Transitional Flow for Hypersonic Reentry Conditons," AIAA Paper No. 84-0223, 1984.

12. Gnoffo, Peter, "Hypersonic Flows over Biconics using a Variable Effective Gamma, Parabolized Navier-Stokes Code," AIAA Paper No. 83-1666, 1983.

13. Jain, A.C. and Prabha, S., " A Comparative Study of Stagnation Point Hypersonic Viscous Shock Layer Flow and Hypersonic Merged Layer Flow," Proc. of the 14th Int. Sym. on Rarefied Gas Dynamics, edited by H. Oguchi, Tsukuba City, Japan, 1984, pp. 241-248.

14. Henricks, W.L, "A Similarity Solution of the Navier-Stokes equations with Wall Calcalysis and Slip for Hypersonic, Low Reynold Number Flow over Spheres," AIAA Paper No. 75-765, 1975.

15. Gupta, R.N., Scott, C.D., and Moss, J.N., "Slip Boundary Equations for Multi-Component Nonequilibrium Airflow," NASA TP-2452, NW., 1985.

16. Johnston, K.D. and Henricks, W.L., "A Numerical Solution of the Naier-Stokes Equations for Chemical Nonequilibriium, Merged Stagnation Shock Layers on Spheres and Two-dimensional Cylinders in Air," NASA TP-1227, May, 1978.

17. Jain, A.C., "Lectures on Reentry Aerodynamics," published by Vikram Sarabbai Space Center, Trivandrum, India, 1980.

18. Kennard, E.H., "Kinetic Theory of Gases," McGraw-Hill Book Co., New York, NY, 1938, pp. 292-295.

19. Potter, J.L. and Bailey, A.B., "Pressures in the Stagnation Region of Blunt Bodies in the Viscous Layer to Merged Layer Regimes of Rarefied Flow," AEDC-TRD-63-168, 1963, Arnold Engineering Development Center, Tullahoma, TN.

20. Ahouse, D.R. and Bogdonoff, S.M., "An Experimental Flowfield Study of the Rarefied Blunt Body Problem," AIAA Paper. No. 69-656, 1969.

21. Russel, D.A., "Density Ahead of a Sphere in Rarefied Supersonic Flow," The Physics of Fluid, Vol. 11, No. 8, 1968, pp. 1679-1685.

22. Kumar, A. and Jain, A.C., "Nonequilibrium Merged Stagnation Shock Layers at Hypersonic Speeds," Int. J. Heat and Mass Transfer, Vol. 18, Oct., 1975, pp. 1113-1118.

23. Wray, K.L., "Chemical Kinetics of High Temperature Air," Hypersonic Flow Research, edited by F.R. Riddel, Academic Press, 1962.

24. Scott, C.D., "Wall Boundary Equations with Slip and Catalysis for Multi-component Nonequilibrium Gas Flows," NASA TM X-58111, 1973.

25. Hendricks, W.L., "Slip Conditions with Wall Catalysis and Radiation for Multicomponent, Nonequilibrium Gas Flow," NASA TM X-64942, June, 1974.

26. Gupta, R.N. and Simmonds, A.L., "Hypersonic Low density Solutions of the Navier-Stokes Equations with Chemical Nonequilibrium and Multi-component Surface Slip," AIAA paper No. 86-1349, 1986.

27. Dellinger, T.C., "Computation of Nonequlibrium Merged Stagnation Shock Layers by Successive Replacement," AIAA J., Vol. 9, 1971, pp. 262-269.

28. Lew, H., "Method of Acceleratd Successive Replacement Applied to Boundary Layer Equations," AIAA J., Vol. 6, No. 5, 1968, pp. 929-931.

29. Pavlov, B.M., "Calculations of Supersonic Flow Past Blunt Bodies Using the Complete Navier-Stokes Equations," Izv. An USSR Machanika Zhidkosti I Graza, Vol. 3, No. 3, 1968, pp. 128-133. Translated in "Fluid Dynamics," Nov. 1967, pp. 88-90.

30. Kitchens, Jr., C.W., "Numerical Experiments with the Compressible Navier-Stokes Equations," Proc. Third Int. Conf. on Numerical Methods in Fluid Dynamics, Orsay, July 3-7, 1972, pp. 120-129.

31. Tassa, Yehuda and Conti, R.J., "Numerical Computations of Hypersonic Laminar Near Wake via Navier-Stokes Solver," AIAA Paper No. 85-1672, July, 1985.

32. Gnoffo, P.A., "A Computational Study of the Flowfield Surrounding the Aeroassist Flight Experiment Vehicle," AIAA Paper No. 87-1575, June, 1987.

33. Dogra, V.K., Moss, J.N. and Simmonds, A.L., "Direct Simulation of Aerothermal Loads for an Aeroassist Flight Experiment Vehicle," AIAA Paper No. 87-1546, June, 1987.

34. Bird, G.A., "Nonequilibrium Radiation During Reentry at 10 km/s," AIAA Paper No. 87-1543, June, 1987.

35. Park, C., "Calculations of Nonequilibrium Radiation in the Flight Regimes of Aeroassisted Orbital Transfer Vehicles," Thermal Design of Aeroassisted Orbital Transfer Vehicles, Progress in Aeronautics and Astronautics, Vol. 96, 1985, pp. 395-418.

36. Jones, J.J., "The Rational for an Aeroassist Flight Experiment," AIAA Paper No. 87-1508, 1987.

37. Krylov, A.A., Banov, B.F. and Starikov, B.B., "Experimental Study of Normal and Tangential Stresses on the Surface of Simple Shape Bodies in Rarefied Flows," 13th Int. Sym. on Rarefied Gas Dynamics, 1982, pp. 495-502.

38. Allegre, J., Raffin, M., and Vennemann, D., "Flow Velocity Determination Along a Wake Axis," 9th Int. Sym. on Rarefied Gas Dynamics, 1974, pp. B.9.1-B.1.10.

39. Koppenwallner, G., "Experimentelle Untersuchung der Druckverteilung und des Widerstands von Querangestromten Kreiszylindern Dei Hypersonischen Machzahlen in Bereich von Kontinuums-bis Freier Molekular-Stromung," Zeitschrift Fur Flugwissen-Chaften, Vol. 17, No. 10, 1969, pp. 321-332.

40. Blankson, I.M. and Finston, Morton, "Measurements in the Laminar Near Wake of Magnetically Suspended Cones at $M_\infty = 6.3$" AIAA J., Vol. 13, No. 12, 1975, pp. 1562-1567.

41. Crane, J.J., "Comments on 'Measurements in the Laminar Near Wake of Magnetically Suspended Cones at $M_\infty = 6.3$,'" AIAA J., Vol. 15, No. 6, 1977, pp. 891-892.

42. Jain, A.C., "Numerical Solutions of Navier-Stokes Equations for the Structure of a Trailing Vortex," NASA TM-X, 73361, Jan. 1977.

APPENDIX

The coefficients in the momentum equations and energy equation, Eqs. (2.11) to (2.13) are as follows:

$$A_1 = \frac{1}{n_e{}^2}\left[\frac{4}{3} + \frac{\eta^2\, n_e'{}^2}{(1 + n_e\eta)^2}\right]$$

$$A_2 = -\frac{2\,\eta\, n_e'}{n_e(1 + n_e\eta)^2}$$

$$A_3 = \frac{1}{(1 + n_e\eta)^2}$$

$$A_4 = -\frac{\eta}{n_e(1 + n_e\eta)^2}\left\{n_e'\,\mathrm{Cot}\,\theta + \frac{n_e'}{\mu}\left(\mu_\theta - \frac{\eta}{n_e}\,n_e'\,\mu_\eta\right)\right.$$

$$\left.-\left(\frac{2n_e'{}^2}{n_e} - n_e''\right)\right\} + \frac{8}{3}\cdot\frac{1}{n_e(1 + n_e\eta)} + \frac{4}{3}\cdot\frac{1}{n_e{}^2}\cdot\frac{1}{\mu}\cdot\frac{\partial\mu}{\partial\eta}$$

$$-\frac{\rho\,R_{eo}}{n_e\,\mu}\left(v - \frac{u}{1 + n_e\eta}\,\eta\, n_e'\right)$$

$$A_5 = \frac{1}{(1 + n_e\eta)^2}\left[\mathrm{Cot}\,\theta + \frac{1}{\mu}\left(\mu_\theta - \frac{n_e'}{n_e}\,\eta\mu_\eta\right)\right] - \frac{\rho\,u}{1 + n_e\eta}\cdot\frac{R_{eo}}{\mu}$$

$$A_6 = -\frac{4}{3}\cdot\frac{1}{\mu(1 + n_e\eta)}\left(\frac{\mu_\eta}{n_e} + \frac{2\mu}{1 + n_e\eta}\right)$$

$$A_7 = \frac{1}{\mu}\,\frac{1}{1 + n_e\eta}\left(\frac{\partial}{\partial\theta} - \frac{n_e'}{n_e}\,\eta\,\frac{\partial}{\partial\eta}\right)\left[\frac{\mu(1 + n_e\eta)}{n_e}\,\frac{\partial}{\partial\eta}\cdot\frac{u}{1 + n_e\eta}\right]$$

$$-\frac{1}{\mu}\cdot\frac{2}{1 + n_e\eta}\left[\frac{1}{3}\cdot\frac{1}{n_e}\left(\mu_\eta - \frac{\mu\,n_e}{1 + n_e\eta}\right) + \frac{\mu}{1 + n_e\eta}\right]\left(u\,\mathrm{Cot}\,\theta + \frac{\partial u}{\partial\theta}\right)$$

$$+ \frac{2}{3} \cdot \frac{1}{\mu} \cdot \frac{1}{n_e(1 + n_e \eta)} \left[\frac{n_e'}{n_e} \eta \left(\mu_\eta - \frac{\mu n_e}{1 + n_e \eta} \right) \right.$$

$$\left. + \mu \left(\frac{n_e'}{n_e} - \cot \theta \right) + \frac{3 \mu_\eta n_e'}{1 + n_e \eta} \right] \frac{\partial u}{\partial \eta}$$

$$- \frac{2}{3} \cdot \frac{1}{n_e} \cdot \frac{1}{1 + n_e \eta} \left[\frac{\partial^2 u}{\partial \eta \partial \theta} - \frac{n_e'}{n_e} \eta \frac{\partial^2 u}{\partial \eta^2} \right] + \frac{\cot \theta}{n_e} \frac{\partial}{\partial \eta} \frac{u}{1 + n_e \eta}$$

$$+ \frac{R_{eo}}{\mu} \left(\frac{\rho u^2}{1 + n_e \eta} - \frac{1}{n_e} \frac{\partial p}{\partial \eta} \right)$$

$$B_1 = \frac{1}{n_e^2} \left(1 + \frac{4}{3} \cdot \frac{n_e'^2}{(1 + n_e \eta)^2} \cdot \eta^2 \right)$$

$$B_2 = - \frac{8}{3} \cdot \frac{n_e'}{n_e(1 + n_e \eta)^2} \cdot \eta$$

$$B_3 = \frac{4}{3} \frac{1}{(1 + n_e \eta)^2}$$

$$B_4 = \frac{4}{3} \cdot \frac{\eta}{n_e(1 + n_e \eta)^2} \left[n_e' \left(\frac{n_e'}{n_e} \eta \frac{\mu_\eta}{\mu} - \frac{\mu_\theta}{\mu} - \cot \theta \right) \right.$$

$$B_5 = \frac{4}{3} \cdot \frac{1}{(1 + n_e \eta)^2} \left[\frac{\mu_\theta}{\mu} - \frac{n_e'}{n_e} \eta \frac{\mu_\eta}{\mu} + \cot \theta \right] - \frac{\rho u}{1 + n_e \eta} \cdot \frac{R_{eo}}{\mu}$$

$$+ \left(\frac{2 n_e'^2}{n_e} - n_e'' \right) \right] + \frac{1}{n_e^2} \cdot \frac{\mu_\eta}{\mu} + \frac{2}{n_e(1 + n_e \eta)}$$

$$+ \frac{R_{eo} \rho}{n_e \mu} \left(\frac{\eta n_e'}{1 + n_e \eta} u - v \right)$$

- 87 -

$$B_6 = -\frac{2}{3} \cdot \frac{1}{(1 + n_e \eta)^2} \left[\frac{\cot\theta}{\mu} \left(\mu_\theta - \frac{n_e'}{n_e} \eta \mu_\eta \right) + 2 \csc^2\theta \right]$$

$$- \frac{1}{n_e} \frac{1}{(1 + n_e \eta)} \cdot \frac{\mu_\eta}{\mu} - \frac{R_{eo}}{\mu(1 + n_e \eta)} \rho v$$

$$B_7 = - \frac{R_{eo}}{\mu(1 + n_e \eta)} \left(\frac{\partial p}{\partial \theta} - \frac{n_e'}{n_e} \eta \frac{\partial p}{\partial \eta} \right) - \frac{1}{3} \cdot \frac{n_e'}{n_e^2 (1 + n_e \eta)} \eta \frac{\partial^2 v}{\partial \eta^2}$$

$$+ \frac{1}{3} \cdot \frac{1}{n_e(1 + n_e \eta)} \frac{\partial^2 v}{\partial \eta \partial \theta}$$

$$+ \frac{1}{1 + n_e\eta} \left(\frac{1}{n_e} \frac{\mu_\eta}{\mu} + \frac{8}{3} \cdot \frac{1}{1 + n_e\eta} \right) \frac{\partial v}{\partial \theta}$$

$$- \frac{1}{1 + n_e\eta} \left[\frac{1}{3} \cdot \frac{1}{n_e\mu} \left(2\mu_\theta + \frac{n_e'}{n_e} \eta\mu_\eta \right) \right.$$

$$\left. + \frac{n_e'}{n_e(1 + n_e \eta)} \left(3\eta + \frac{1}{3n_e} \right) \right] \frac{\partial v}{\partial \eta}$$

$$+ \frac{2}{3\mu(1 + n_e \eta)^2} \left(\mu_\theta - \frac{n_e'}{n_e} \eta \mu_\eta \right) v$$

$$C_1 = \frac{\mu}{n_e^2(1 + n_e \eta)} \left[(1 + n_e \eta) + \frac{n_e'^2}{1 + n_e\eta} \eta^2 \right] \cdot \frac{\Lambda}{R_{eo}} \cdot \frac{1}{Pr}.$$

$$C_2 = - \frac{2\mu}{(1 + n_e\eta)^2} \frac{n_e'}{n_e} \eta \frac{\Lambda}{Re_o} \frac{1}{Pr}$$

$$C_3 = \frac{\mu}{(1 + n_e\eta)^2} \frac{\Lambda}{Re_o} \frac{1}{Pr}$$

$$C_4 = \frac{\mu}{n_e(1 + n_e\eta)} \left\{ 2 + (1 + n_e\eta)\frac{\mu_\eta}{\mu} \right.$$

$$\left. - \frac{\eta}{1 + n_e\eta} \left[n_e'' - 2\frac{n_e'^2}{n_e} + n_e'\cot\theta + \frac{n_e'}{\mu}\left(\mu_\theta - \frac{n_e'}{n_e}\eta\mu_\eta \right) \right] \right\} \frac{\Lambda}{Re_o\ Pr}$$

$$- \rho\frac{\Lambda}{n_e}\left(v - \frac{n_e'}{1 + n_e\eta}\eta u \right)$$

$$C_5 = \frac{\mu}{(1 + n_e\eta)^2}\left[\cot\theta + \frac{1}{\mu}\left(\mu_\theta - \frac{n_e'}{n_e}\eta\mu_\eta \right) \right] \frac{\Lambda}{Re_o\ Pr}$$

$$-, \frac{\rho\Lambda}{1 + n_e\eta}\ u$$

$$C_6 = 0.0$$

$$C_7 = \frac{\mu}{Re_o}\left\{ \frac{2}{n_e^2}\left(\frac{\partial v}{\partial \eta} \right)^2 + \frac{2}{(1 + n_e\eta)^2}\left(v + \frac{\partial u}{\partial \theta} - \frac{n_e'}{n_e}\eta\frac{\partial u}{\partial \eta} \right)^2 \right.$$

$$+ \frac{2}{(1 + n_e\eta)^2}(v + u\cot\theta)^2 + \left[\frac{1}{n_e}\left(\frac{\partial u}{\partial \eta} - \frac{n_e}{1 + n_e\eta}u \right) \right.$$

$$\left. + \frac{1}{1 + n_e\eta}\left(\frac{\partial v}{\partial \theta} - \frac{n_e'}{n_e}\eta\frac{\partial v}{\partial \eta} \right) \right]^2$$

$$- \frac{2}{3}\frac{1}{(1 + n_e\eta)^2}\left[2v + \frac{1 + n_e\eta}{n_e}\cdot\frac{\partial v}{\partial \eta} + u\cot\theta \right.$$

$$\left. + \left(\frac{\partial u}{\partial \theta} - \frac{n_e'}{n_e}\eta\frac{\partial u}{\partial \eta} \right) \right]^2 \right\} + \left(v - \frac{n_e'}{1 + n_e\eta}\eta u \right)\frac{1}{n_e}\frac{\partial p}{\partial \eta} + \frac{u}{1 + n_e\eta}\frac{\partial p}{\partial \theta}$$

- 89 -

C-2

ACKNOWLEDGEMENTS